

# Weld line recognition and path planning with spherical tank inspection robots

Jie Li<sup>1</sup>  | Shanshan Jin<sup>1</sup> | Cunjin Wang<sup>1</sup> | Jiameng Xue<sup>2</sup> | Xingsong Wang<sup>1</sup>

<sup>1</sup>Department of Mechanical and Electronic Engineering, School of Mechanical Engineering, Southeast University, Nanjing, China

<sup>2</sup>Department of Electric and Electronic Engineering, School of Engineering, The University of Manchester, Manchester, UK

## Correspondence

Xingsong Wang, Department of Mechanical and Electronic Engineering, School of Mechanical Engineering, Southeast University, Nanjing 211189, China.  
Email: [xswang@seu.edu.cn](mailto:xswang@seu.edu.cn)

## Funding information

The National Prevention Key Technology Project for Serious and Major Accidents in Work Safety of China, Grant/Award Number: No. Jiangsu-0002-2017AQ; The Science and Technology Project of Quality and Technical Supervision Bureau of Jiangsu Province, China, Grant/Award Number: KJ175933

## Abstract

Periodic inspections are required for the safe operation of large pressure vessels such as spherical tanks. Inspection robots have been applied in large pressure vessels due to their low cost and high efficiency. This paper presents a robotic system for the inspection of spherical tanks, which can identify and track weld lines on the shortest running route. Two-dimensional (2D) weld maps were prepared for robot path planning on the basis of the actual distribution of weld lines. In 2D weld maps, indispensable repetitive lines were added to form an Eulerian circuit that traversed all weld lines. In addition, an improved Fleury algorithm was proposed to solve Eulerian circuit and plan an optimal running route for robot inspection. To accurately identify weld lines, deep learning networks were constructed and trained with weld line data sets, which were captured by the camera mounted in the front of the robot. The laboratory experiments indicated that the inspection robot could identify weld lines within 0.2–0.25 s and track weld lines with a maximum offset of  $\pm 20$  mm. The experiment results demonstrated that the robot could plan the shortest path to traverse all weld lines on the experimental platform. In the field tests, the virtual simulation of weld path planning on spherical tanks was explored in detail. The field tests of a spherical tank ( $3000\text{ m}^3$ ) verified that the robotic system could improve the efficiency and stability of inspection operations and replace manual inspection with automated weld line recognition and weld path planning.

## KEY WORDS

climbing robot, inspection robot, path planning, weld line recognition

## 1 | INTRODUCTION

Spherical tanks are spherical steel pressure vessels for storing liquefied petroleum gas (LPG), which are widely applied in petroleum, chemical, metallurgical, and other fields. Spherical tanks are welded from multiple cambered plates, as a result of this, weld lines are distributed on their surface. These lines may generate cracks, pits, holes, and other defects due to the affection of pressure, temperature, corrosion, and so on. Weld defects can cause chemical leakage, fire, explosion, casualties, and huge economic losses, so weld lines of spherical tanks must be inspected and repaired regularly.

Many inspection robots have been designed to take the place of manual tests (Faruq Howlader & Sattar, 2015; Fernández et al., 2010; La et al., 2019; Leon-Rodriguez et al., 2012; B. Li et al., 2017; Oliveira et al., 2010; Tâche et al., 2009). They can save detection cost, improve the detection efficiency, and eliminate safety risks of workers. Wall-climbing robots can carry a variety of devices and instruments for inspections (Ding et al., 2019; Sogi et al., 2000).

In the robotic inspection process of spherical tanks, high-precision localization and navigation can improve the operation efficiency and accuracy of inspection robots. Inspection robots running on spherical tank surface involve three-dimensional (3D) positioning.

However, due to different materials and structures of spherical tanks, it is difficult to achieve high positioning accuracy with conventional localization technologies, such as global positioning system and inertial measurement unit estimation (Kim & Lee, 2016), and mileage accumulation. A variety of sensors, such as vision sensors, depth cameras (Espinoza et al., 2015; Teixeira et al., 2018), lidars, and infrared distance sensors, have been used for robot positioning. Usually, a single sensor often cannot achieve high-precision positioning and the multisensor positioning fusion method can increase the accuracy and reliability of robot positioning.

Weld lines are the detection objects on spherical tanks and weld line recognition is an important task of inspection robots. By tracking weld lines, inspection robots can autonomously correct the running routes and perform inspection continuously. Different kinds of robots have been developed to extract and calculate weld lines. For example, an inspection robot scanning and locating weld lines with a lidar sensor (Da Veiga et al., 2016), a climbing robot detecting weld lines via a cross structured light (CSL) device (L. Zhang, Ke, et al., 2014; L. Zhang, Ye, et al., 2014), a robotic weld line tracking system based on dual cameras (Z. Wang et al., 2017) and some weld detection robots based on image processing techniques (Rout et al., 2019). Images are easily affected by light and environment, which leads to the low accuracy of image recognition. In recent years, neural networks and deep learning have been introduced into weld line recognition (Günther et al., 2016; Kim & Cho, 2019; Lin et al., 2018; Sassi et al., 2019) and have greatly improved the recognition accuracy. However, the training process of deep learning is complicated and time-consuming.

Multiple intersecting weld lines are distributed on the surface of spherical tanks. Optimal path planning can improve the efficiency of inspection robots. Different running paths are planned based on task requirements and constraint criteria, such as the shortest time, the shortest distance, and full traversal. To solve path planning problems in different situations, many methods have been proposed, such as template matching, artificial potential field, map construction and neural networks. Since weld lines of spherical tanks are irregularly

distributed in 3D space, optimal path planning for inspection robots should meet the following conditions: traversing all the weld lines, the shortest distance and returning to the starting point.

So far, we have developed some wall-climbing robots (J. Li & Wang, 2016; Tu et al., 2017; Zheng et al., 2016), which can achieve stable operation on inner and outer surfaces of spherical tanks. In addition, some recognition and positioning methods for weld lines have been proposed (Liang et al., 2016, 2017; S. Wang & Wang, 2016). To solve the positioning and navigation problems of spherical tank inspection robots, a novel approach of positioning and navigation was proposed in the study. We explored a weld line tracking method based on deep learning, as well as an optimal path planning method for traversing all weld lines of spherical tanks. With a deep learning model based on convolutional neural networks (CNNs), weld lines in captured images were successfully identified. Based on the combined method of image processing and path fitting, weld paths were extracted for robot guidance. In terms of robot path planning, weld path maps were prepared and repetitive paths were added. Finally, an Eulerian circuit was solved to achieve the shortest path planning and traversal all weld lines on spherical tanks.

## 2 | SPHERICAL TANK INSPECTION ROBOT

### 2.1 | Robot mechanism design

An inspection robot was developed to carry nondestructive testing (NDT) equipment and repair tools to inspect and maintain weld seams on spherical tanks. As shown in Figure 1, the robot consists of an adjustable body, shock-absorbing suspensions, magnetic adsorption units, mecanum wheels, a weld line recognition component.

The curvature of the inspection robot can be changed through the adjustable body so as to be adapted to spherical tank surfaces with different diameters. The shock-absorbing suspension endows

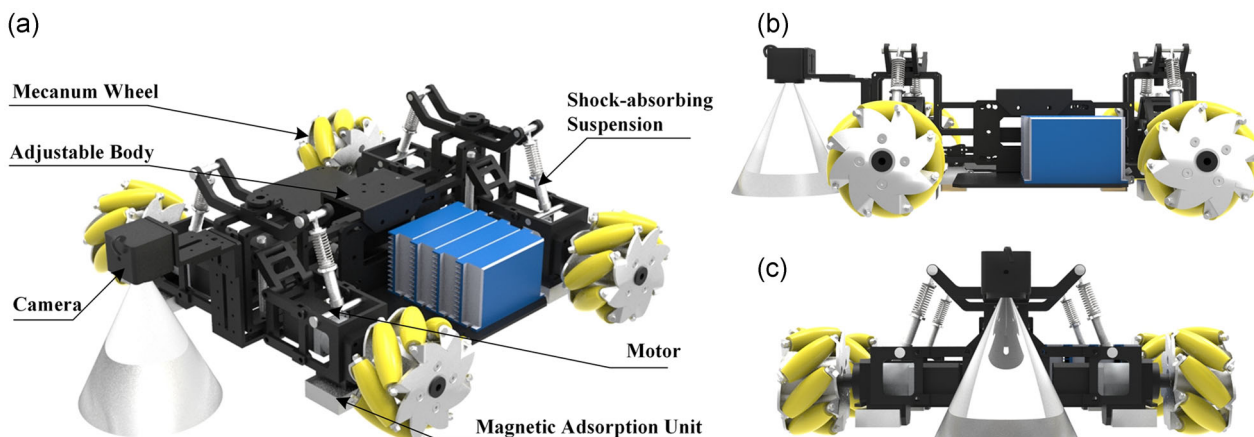


**FIGURE 1** Spherical tank inspection robot: (a) overall view; (b) side view; (c) front view

the robot with a stronger ability to negotiate welds and other obstacles smoothly. With four mecanum wheels, the robot can perform omni-directional movement on the surface of spherical tanks, thus greatly enhancing its flexibility. The permanent magnet units near mecanum wheels provide magnetic adsorption force for the robot and its position varies with the angle of the adjustable body. The mechanical design and force analysis of the robot have been analyzed and reported (J. Li et al., 2019).

The weld line recognition component is composed of an adjustable vertical bracket, two adjustable horizontal brackets and an industrial camera. The camera, with wide-angle lens and 38 mm focal distance, is used to capture stable and distortionless weld images.

The main performance parameters of the inspection robot are shown in Table 1 and Figure 2. The self-weight of the robot is 13.75 kg and the adsorption force of each magnetic adsorption unit is 204 N. Its maximum payload and maximum climbing speed are 10 kg and 0.2 m/s, respectively.

**TABLE 1** Parameters of the inspection robot

Dimension	466 × 520 × 198 mm
Mass	13.75 kg
Payload	10 kg
Maximum climbing speed	0.2 m/s
Motor power	60 W
Obstacle-negotiation capability	5 mm
Adsorption force	204 N
Working time	120 min

## 2.2 | Additional machineries

Based on the inspection robot, we have designed and applied a variety of additional tools and equipment to detect and maintain spherical tanks. The automation operations performed by the robot include flaw detection, grinding and cleaning. As shown in Figure 3a, the NDT machinery includes a lifting motor, two elastic slide rails, and two ultrasonic probes. The lifting motor can change the height of the ultrasonic probes. Based on the time of flight diffraction (TOFD) method (Spies et al., 2012) and ultrasonic signals, the internal defects of weld seams can be found. The grinding machinery (Figure 3b) and the cleaning machinery (Figure 3c) can be easily installed on the robot to perform maintenance operations. A host computer is used to process data and execute some real-time algorithms.

## 2.3 | Robot inspection tasks

The weld seam must be inspected regularly to ensure the safe operation of spherical tanks, so inspection robots need to run and track along weld seams, carrying testing equipment and maintain tools. Autonomous navigation and positioning is essential for inspection robots. As one of positioning methods, automatically tracking weld lines by the robot can effectively replace manual operations and be conducive to saving time and energy. The running route of the robot is determined by the position and distribution of these weld lines. There are many weld lines on spherical tanks and they intersect each other, so finding an optimal path is necessary to improve its work efficiency. The main tasks of the robot are provided as follows:

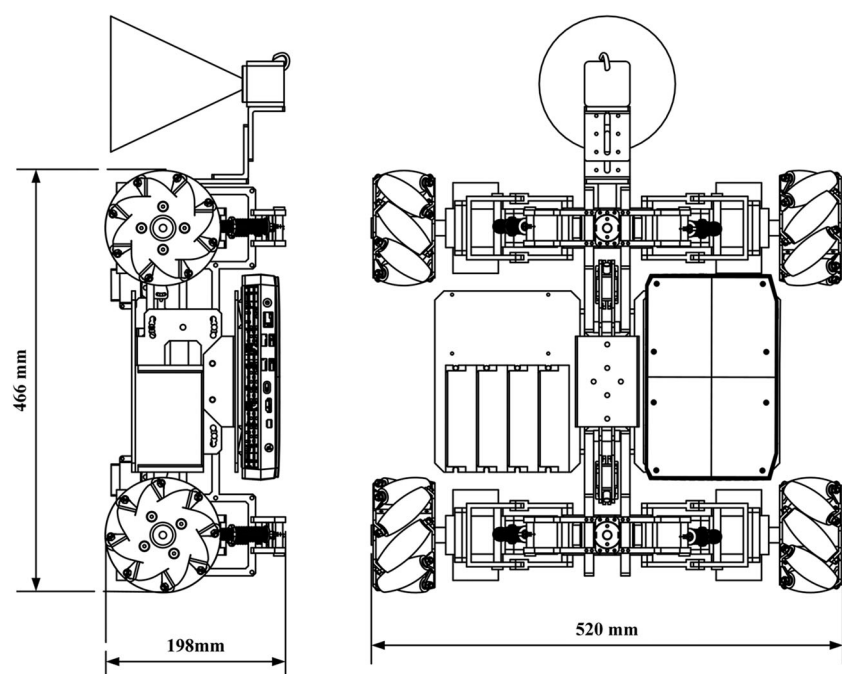


**FIGURE 2** Dimensional drawing of the robot

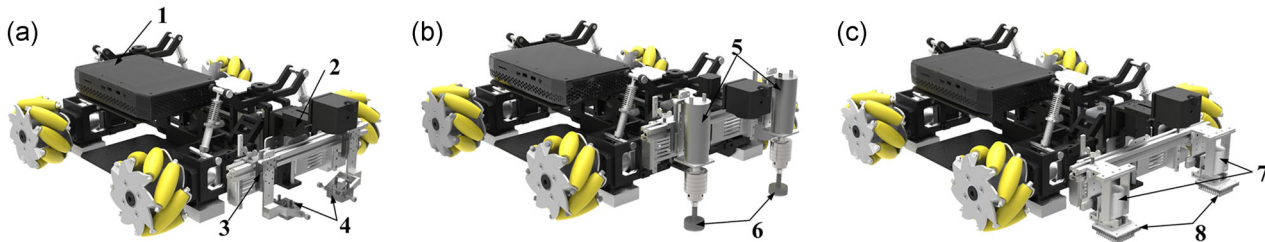
- (1) Stable running on the surface of the spherical tank;
- (2) Preparing weld line maps and finding an optimal path that traverses all weld lines with the shortest total distance;
- (3) Recognizing and extracting weld lines;
- (4) Selecting and tracking planned weld paths;
- (5) Inspecting and maintaining weld lines.

### 3 | PREPARATION OF WELD MAPS

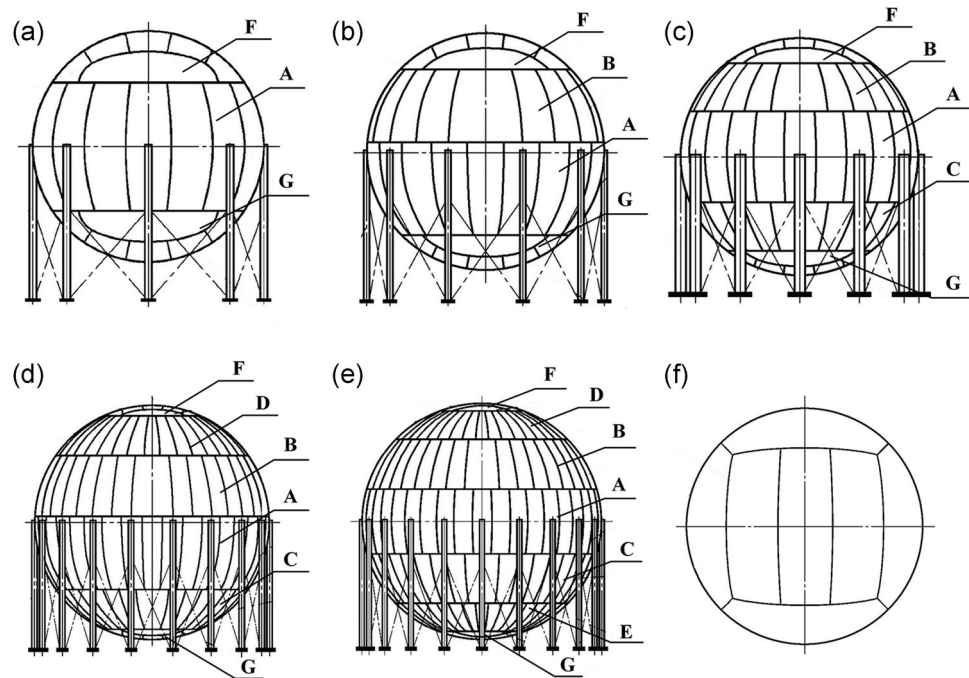
Generally, spherical tanks are welded from many cambered plates and the distribution position of weld lines can be calculated based on its design parameters. Weld maps were prepared to analyze position distribution of weld lines, plan robot's running route and show robot's position coordinates.

### 3.1 | Weld line distribution

Spherical tanks are usually store LPG and other industrial and chemical substances. Due to the advantages of large volume and high pressure, hybrid-type spherical tanks are widely used in the petrochemical field. Hybrid-type spherical tanks must be designed and assembled in accordance with national standards (such as GB/T 17261-2011 "Steel spherical tanks type and dimension data base," in China). The hybrid-type spherical tanks are composed of multiple zones, of which the top zone and the bottom zone are welded by multiple plates. As shown in Figure 4, according to the number of zones, the hybrid spherical tanks are divided into five types, which are three-zones type, four-zones type, five-zones type, six-zones type and seven-zones type. The zones on the spherical tanks include **F**-zone, **D**-zone, **B**-zone, **A**-zone, **C**-zone, **E**-zone, and **G**-zone, representing the upper polar zone, the upper



**FIGURE 3** Robot additional machineries: (a) NDT machinery: 1—host computer, 2—lifting motor, 3—elastic slide rails, and 4—ultrasonic probes; (b) grinding machinery: 5—motors and 6—grinding head; (c) cleaning machinery: 7—motors and 8—cleaning brushes

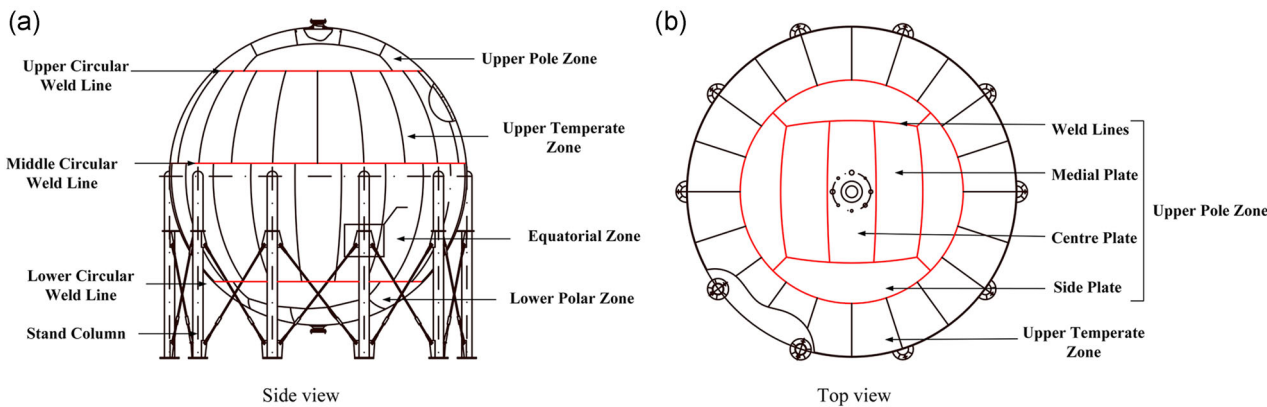


**FIGURE 4** Hybrid-type spherical tanks: (a) three-zones type, (b) four-zones type, (c) five-zones type, (d) six-zones type, (e) seven-zones type, and (f) weld distribution in F-zone and G-zone

**TABLE 2** Volume and parameters of hybrid-type spherical tanks

Volume (m <sup>3</sup> )	Diameter (m)	Zone number	Plates number in different zone						
			F-Zone	D-Zone	B-Zone	A-Zone	C-Zone	E-Zone	G-Zone
1000	12.3	3	7	-	-	16	-	-	7
1500	14.2	3/4	7	-	-/20	16/20	-	-	7
2000	15.7	3/4	7	-	-/20	16/20	-	-	7
3000	18.0	3/4	7	-	20/24	20/24	-	-	7
4000	19.7	4/5	7	-	20/24/28	20/24/28	-/28	-	7
5000	21.2	4/5	7	-	24/28	24/28	24/28	-	7
6000	22.6	5	7	-	24/28	24/28	24/28	-	7
...	...	...	...	...	...	...	...	...	7
23000	35.3	6	7	36	36	36	36	36	7
25000	36.3	6/7	7	36/30	36/40	36/40	36/40	-/30	7

Note: "/" represents "or" and "-" represents "null".

**FIGURE 5** Composition and weld distribution of the spherical tank. (a) Side view and (b) top view

frigid zone, the upper temperate zone, the equatorial zone, the lower temperate zone, the lower frigid zone and the lower polar zone. The upper pole zone and the lower pole zone plate have the same welding form and consists seven plates (Figure 4f).

As shown in Table 2, as the volume of spherical tanks increases, the number of zones is different. For example, 1000-m<sup>3</sup> spherical tanks generally consist of three zones, and 3000-m<sup>3</sup> spherical tanks are composed of six or seven zones. Although there are many types of spherical tanks, their weld line distribution and position are similar and regular. We can easily create and build similar weld maps for different spherical tanks.

### 3.2 | 2D weld maps

To search for the shortest running path, the weld lines on 3D spherical tanks are mapped to 2D maps and their parameters includes relative position and length. Taking hybrid-type spherical tanks with four-zones as an example (Figure 5): the equatorial zone and the

upper temperate zone of the spherical tank are respectively composed of 20 symmetrical cambered plates; the upper polar zone and the lower polar zone are respectively composed of seven cambered plates with different directions and sizes.

According to the distribution characteristic of weld lines, 2D maps used for path planning include a middle zone map, an upper pole zone map, and a lower pole zone map. As shown in Figure 6, the middle zone map contains the equatorial zone and the upper temperate zone.

To distinguish weld line intersections, these intersections in 2D weld maps are recorded as Points  $A_i-G_j$ . According to the distribution of weld lines, their subscripts range from 0 to 103, which indicates the serial numbers of weld intersections.

In the middle zone map, Circle A represents the upper circular weld line between the upper temperate zone and the upper polar zone; Circle B represents the middle circular weld line between the upper temperate zone and the equatorial zone; Circle C represents the lower circular weld line between the equatorial zone and the lower polar zone. Line Segments  $A_iB_j$  and  $B_iC_j$ , respectively represent

longitudinal weld lines in the upper temperate zone and the equatorial zone. Line Segments  $A_iA_j$ ,  $B_iB_j$  and  $C_iC_j$ , respectively represent transverse weld lines between weld intersections in Circles A, B, and C. The length relationship between line segments in the middle zone map is shown in Table 3.

In the upper pole zone map (Figure 7), four points  $F_i$  represent the weld intersections between the upper pole zone and the upper temperate zone (not coincident with Points  $A_i$ ) and other intersections are

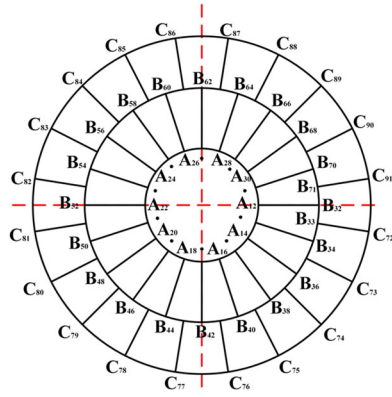


FIGURE 6 Middle zone map

TABLE 3 Length relationship between line segments in the middle zone map

Line segments	$A_iA_j$	$A_iB_j$	$B_iB_j$	$B_iC_j$	$C_iC_j$
Length ( $\pi R$ )	0.0707	0.2220	0.0489	0.2779	0.0707

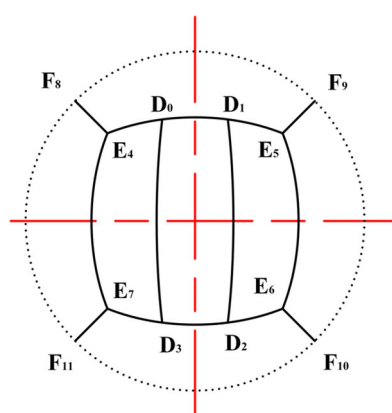


FIGURE 7 Upper pole zone map

represented as  $D_i$  and  $E_i$ . The length relationship between line segments in the upper pole zone map is shown in Table 4. The lower pole zone map is similar to the upper pole zone map, as shown in Figure 8.

## 4 | WELD PATH PLANNING

Since the distribution of weld lines on spherical tanks is intricate, an optimal path can improve robot inspection efficiency. According to the design standard of spherical tanks, the distribution of weld lines on its surface is known and the path planning can be determined before robot inspection. The limiting conditions of the optimal weld path planning are provided as follows:

- (1) All weld lines are traversed;
- (2) The shortest total distance.

### 4.1 | Path planning problem

Weld path planning can be seen as a special problem in discrete mathematics and graph theory, similar to "The Chinese Postman Problem" (Eiselt et al., 1995). In mathematical language, the problem can be described as follows:

It is supposed that undirected connected graph,  $G = [V, E, \text{Wt}()]$ , is composed of Point Set  $V$  and Edge Set  $E$ . As for all edges  $e_i \in E$ , corresponding weight  $\text{Wt}(e_i) \geq 0$ . The goal of path planning is to find an optimal path  $\pi$  in the graph, which traverses each edge at least once and satisfies the condition that weight sum  $\sum_{e_i \in \pi} \text{Wt}(e_i)$  is the smallest.

In this problem, if the number of edges connected any point in the undirected graph,  $G$  is even, starting from any point, one Eulerian circuit,

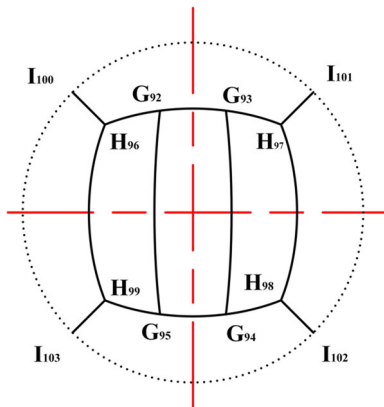
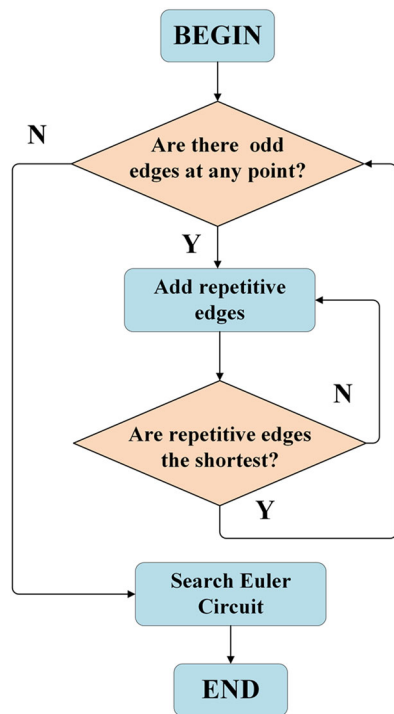


FIGURE 8 Lower pole zone map

Line segments	$E_iF_j$	$D_0D_1, D_2D_3$	$D_iE_j$	$D_0D_3, D_1D_2, E_4E_7, E_5E_6$	$F_iF_j$
Length ( $\pi R$ )	0.0645	0.0806	0.0967	0.2546	0.3537

TABLE 4 Length relationship between line segments in the upper pole zone map



**FIGURE 9** Flowchart for solving the optimal path

which traverse all edges of Graph  $G$ , is necessarily to be found. In fact, multiple Euler circuits, which are all solutions to the problem, may exist.

When the number of edges connected some points is odd, adding repetitive edges (their set is  $E'$ ) between these points can get a new graph,  $G' = G + E'$ , in which odd edges at any point does not exist. The problem is transformed into finding appropriate  $E'$  to ensure that the Eulerian circuit of  $G'$  is the shortest.

In optimal weld path planning,  $Wt(e_i)$  represents the length of each weld path. Some repetitive running routes shall be added to ensure that the number of routes connected any weld intersection is even. Figure 9 is the flowchart for solving the optimal running path.

## 4.2 | Addition of repetitive edges

In the 2D weld maps of the spherical tank, all weld intersections are connected to odd edges (weld lines), such as 12 intersections in the upper pole zone map and 80 intersections in the middle zone map. It is necessary to pair these intersections and add repetitive edges to form Eulerian circuit that traverses all edges.

Although there are many points with odd edges, the weld maps are symmetric and ordered and only several types of edge lengths exist. Combined with the minimum weight match algorithm, we proposed an improved graphical method based on an odd-even-point approach. The method starts from the edge with the smallest weight (representing length), pairs all points with odd edges and search the shortest repetitive edges. The basic steps of the method are provided as follows:

- Removing all points with even edges in Graph  $G = [V, E, Wt()]$ , saving other points and their connected edges to form new graph  $G'$  and creating Edge Set  $P$  to store repetitive edges;
- Searching for Edge  $e(v_i, v_j)$  with the smallest weight from Graph  $G'$ ;
- Adding Edge  $e(v_i, v_j)$  to Edge Set  $P$ , deleting Point  $v_i$ , Point  $v_j$  and edges connected to them from Graph  $G'$ , and adding a corresponding edge to ensure that the shortest path between other points in Graph  $G'$  is consistent with before deleting.
- Judging whether Graph  $G'$  is a null-set: if not, go to Step (e), otherwise, go to Step (f);
- Judging whether Graph  $G'$  is connected, if not, go to Step (b), otherwise, go to Step (f);
- After pairing the points with odd edges, Edge Set  $P$  is the set of all repetitive edges to be solved.

Due to the symmetry of the weld maps, in the process of adding repetitive edges, multiple pairs of points can be found at one time, thus greatly improving the efficiency of solving Edge Set  $P$ .

Figure 10 shows the process of adding repetitive edges to the upper pole zone map. Dotted lines represent the added repetitive edges. The first step is to find four shortest edges (Line Segment  $E_iF_j$ ), pair their corresponding points and add repetitive edges. Then, four pairs of points  $(4, 8), (5, 9), (6, 10), (7, 11)$  and their connected edges are deleted. Similarly, the second step is to add two shortest repetitive edges in the map. Figure 10c shows the final result. Similarly, repetitive edges are also added in the lower pole zone map, as shown in Figure 11.

The process of adding repetitive edges in the middle zone map is shown in Figure 12. The first step is to pair all points  $(B_i, 32 \leq i \leq 71)$  on Circle B, add 20 shortest repetitive edges and delete these points and edges connected to them. To avoid changing the shortest path length between other points, 40 line segments  $(A_iC_j)$  are added between points on Circles A and C. Taking Points  $A_{12}$  and  $C_{91}$  as examples, the shortest path length satisfies the equation:  $A_{12}C_{91} = A_{12}B_{32} + B_{32}B_{71} + B_{71}C_{91}$ . For Points  $A_{12}$  and  $C_{90}$ ,  $A_{12}C_{90} = A_{12}C_{91} + C_{91}C_{90}$ . In Figure 12b, the shortest path length between every two points is consistent with that in Figure 12a. The length between two adjacent points on Circle A (and Circle C) is the shortest, so these points are paired and 20 repetitive edges are added in the second step. Figure 12c shows the final result.

## 4.3 | Eulerian circuit solution

After adding repetitive edges reasonably, a new undirected connected graph can be obtained. In the graph, any Eulerian circuit is the shortest running route. Here, an Eulerian circuit is solved by the Fleury algorithm (B. Zhang & Peng, 2012). The mathematical description of the algorithm is provided as follows:

- In undirected Euler graph,  $G = (V, E)$ , Point  $v_0$  is chosen as the starting point of Path  $P$ , and  $P_0 = v_0$ ;

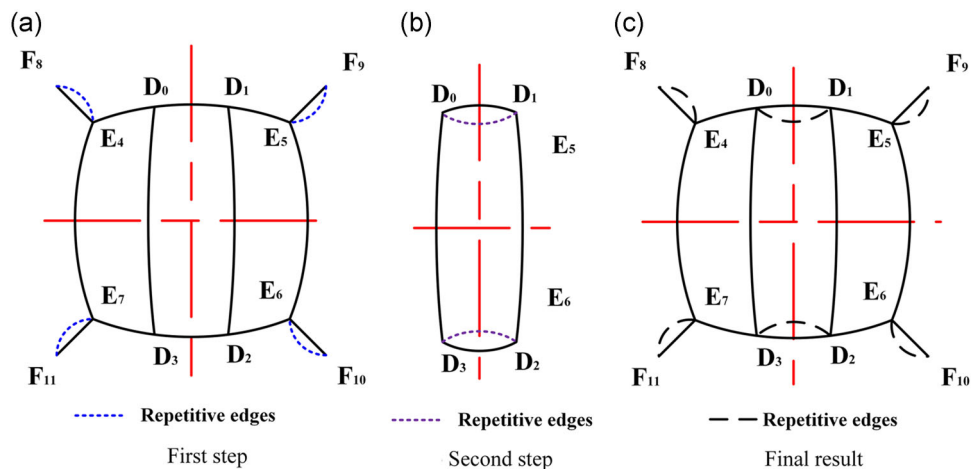


**FIGURE 10** Steps of adding repetitive edges in the upper pole zone map. (a) first, (b) second, and (c) third steps

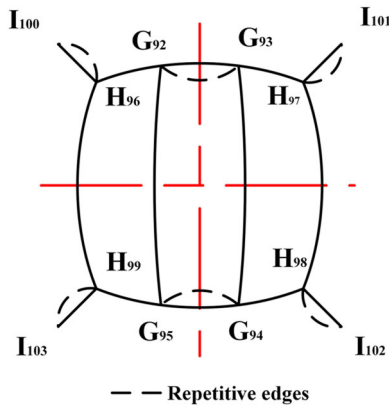


**FIGURE 11** Repetitive edges in the lower pole zone map

- (b) Suppose that a path from Point  $v_0$  to Point  $v_i$  is  $P_i = v_0e_1v_1 \dots e_iv_i$ , then Edge  $e_{i+1}$  is selected from  $E - \{e_1, e_2, \dots, e_i\}$ , which is connected to  $v_i$  and should not be a "bridge" of  $G_i = G - \{e_1, e_2, \dots, e_i\}$  unless there is no choice.  
 (c) When step (b) cannot be executed, the algorithm stops.

The "bridge" refers to a special edge since deleting this edge will cause a connected graph to be unconnected.

For weld maps with repetitive edges, we propose an improved Fleury algorithm to search for an Eulerian circuit. The flowchart of the improved Fleury algorithm is shown in Figure 13. In the algorithm, adjacency matrix  $\text{Edge}[n][n]$  represents the weld map with repetitive edges, and  $n$  represents the serial number of the points in the map.  $\text{Edge}[i][j]$  represents the connection state between Points  $i$  and  $j$ . Its values are 0, 1, and 2. In the solution procedure, the running path starts from a point and visits adjacent points in turn. Every time an edge is visited, corresponding value of  $\text{Edge}[i][j]$  is reduced by 1 and other unvisited edges are saved. When a bridge is visited, the

algorithm first outputs the edges of the undirected connected subgraph connected to this bridge in sequence, and searches for and outputs other undirected connected subgraphs.

In the upper pole zone map, if the selected starting point is  $F_8$ , the Eulerian path solved by the algorithm is:  $8 \rightarrow 4 \rightarrow 7 \rightarrow 11 \rightarrow 7 \rightarrow 3 \rightarrow 2 \rightarrow 6 \rightarrow 10 \rightarrow 6 \rightarrow 5 \rightarrow 9 \rightarrow 5 \rightarrow 1 \rightarrow 2 \rightarrow 3 \rightarrow 0 \rightarrow 1 \rightarrow 0 \rightarrow 4 \rightarrow 8$ . In Figure 14, the blue arrows represent directions of robot running route, which traverses all edges exactly once. In fact, starting from any point and following blue arrows in the map, an Eulerian path is necessarily obtained.

In the middle zone map, if the selected starting point is Point  $A_{12}$ , the Eulerian path solved by the algorithm is:  $12 \rightarrow 32 \rightarrow 71 \rightarrow 70 \rightarrow 69 \rightarrow 68 \rightarrow 69 \rightarrow 90 \rightarrow 91 \rightarrow 90 \rightarrow 89 \rightarrow 88 \rightarrow 89 \rightarrow 67 \rightarrow 66 \rightarrow 65 \rightarrow 64 \rightarrow 65 \rightarrow 88 \rightarrow 87 \rightarrow 86 \rightarrow 87 \rightarrow 63 \rightarrow 62 \rightarrow 61 \rightarrow 60 \rightarrow 61 \rightarrow 86 \rightarrow 85 \rightarrow 84 \rightarrow 85 \rightarrow 59 \rightarrow 58 \rightarrow 57 \rightarrow 56 \rightarrow 57 \rightarrow 84 \rightarrow 83 \rightarrow 82 \rightarrow 83 \rightarrow 55 \rightarrow 54 \rightarrow 53 \rightarrow 52 \rightarrow 53 \rightarrow 82 \rightarrow 81 \rightarrow 80 \rightarrow 81 \rightarrow 51 \rightarrow 50 \rightarrow 49 \rightarrow 48 \rightarrow 49 \rightarrow 80 \rightarrow 79 \rightarrow 78 \rightarrow 79 \rightarrow 47 \rightarrow 46 \rightarrow 45 \rightarrow 44 \rightarrow 45 \rightarrow 78 \rightarrow 77 \rightarrow 76 \rightarrow 77 \rightarrow 43 \rightarrow 42 \rightarrow 41 \rightarrow 40 \rightarrow 41 \rightarrow 76 \rightarrow 75 \rightarrow 74 \rightarrow 75 \rightarrow 39 \rightarrow 38 \rightarrow 39 \rightarrow 40 \rightarrow 16 \rightarrow 17 \rightarrow 42 \rightarrow 43 \rightarrow 44 \rightarrow 18 \rightarrow 19 \rightarrow 46 \rightarrow 47 \rightarrow 48 \rightarrow 20 \rightarrow 21 \rightarrow 50 \rightarrow 51 \rightarrow 52 \rightarrow 22 \rightarrow 23 \rightarrow 54 \rightarrow 55 \rightarrow 56 \rightarrow 24 \rightarrow 25 \rightarrow 58 \rightarrow 59 \rightarrow 60 \rightarrow 26 \rightarrow 27 \rightarrow 62 \rightarrow 63 \rightarrow 64 \rightarrow 28 \rightarrow 29 \rightarrow 66 \rightarrow 67 \rightarrow 68 \rightarrow 30 \rightarrow 31 \rightarrow 70 \rightarrow 71 \rightarrow 91 \rightarrow 72 \rightarrow 73 \rightarrow 74 \rightarrow 37 \rightarrow 36 \rightarrow 37 \rightarrow 38 \rightarrow 15 \rightarrow 14 \rightarrow 36 \rightarrow 35 \rightarrow 34 \rightarrow 35 \rightarrow 72 \rightarrow 33 \rightarrow 32 \rightarrow 33 \rightarrow 34 \rightarrow 13 \rightarrow 14 \rightarrow 15 \rightarrow 16 \rightarrow 17 \rightarrow 18 \rightarrow 19 \rightarrow 20 \rightarrow 21 \rightarrow 22 \rightarrow 23 \rightarrow 24 \rightarrow 25 \rightarrow 26 \rightarrow 27 \rightarrow 28 \rightarrow 29 \rightarrow 30 \rightarrow 31 \rightarrow 12 \rightarrow 13 \rightarrow 12$ .

Figure 15 shows path directions at the beginning of robot running route. The running route follows a certain rule, such as the partial path marked by green arrows ( $89 \rightarrow 88 \rightarrow 89 \rightarrow 67 \rightarrow 66 \rightarrow 65 \rightarrow 64 \rightarrow 65 \rightarrow 88 \rightarrow 87$ ) and the partial path marked by purple arrows ( $87 \rightarrow 86 \rightarrow 87 \rightarrow 63 \rightarrow 62 \rightarrow 61 \rightarrow 60 \rightarrow 61 \rightarrow 86 \rightarrow 85$ ). In the 2D weld maps, starting from any point, at least an Euler circuit can be obtained as the shortest running route for robot inspection.

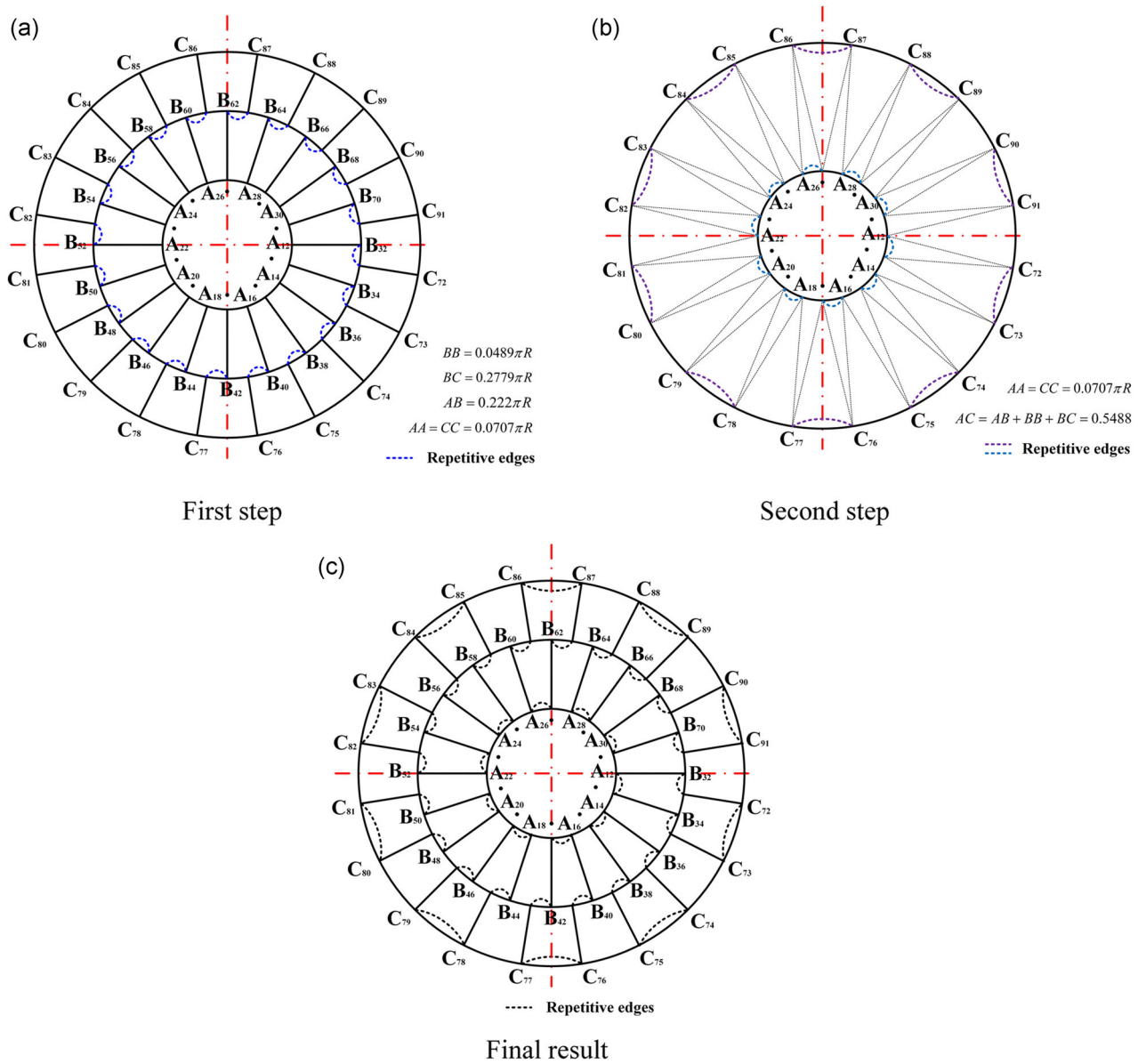


**FIGURE 12** Process of adding repetitive edges in the middle zone map. (a) first, (b) second, and (c) third steps

## 5 | WELD LINE RECOGNITION

Since there is no obvious color difference between weld lines and their surrounding environment, it is difficult to identify and position weld lines only through image processing. After long-term outdoor services, drench and insulation, corrosion and rust may appear on the steel surface of spherical tanks, thus leading to misrecognition and low recognition accuracy of weld lines in image processing. Figure 16 shows weld line images on a storage tank captured by our inspection robot and there are a lot of rust and corrosion around weld lines. The types of weld lines include: single transverse weld lines, single longitudinal weld lines, T-shaped weld lines, and cross-shaped weld lines.

Deep learning provides new means for weld recognition and it is conducive to promoting the automation of inspection robots. We

have tested multiple image processing (Liang et al., 2017), neural networks (S. Wang & Wang, 2016), classification algorithms (Ren et al., 2017) and instance segmentation algorithms for weld recognition. Compared with image processing, CNNs can classify objects more accurately after learning and training. The instance segmentation algorithms have more advantages in pixel segmentation and weld path accuracy. Table 5 shows speed-performance and mask mean average precision (Mask mAP) of different instance segmentation algorithms on COCO test-dev. Compared with PA-Net (Liu et al., 2018), RetinaMask (Fu et al., 2019) and FCIS (Y. Li et al., 2016), Mask R-CNN (He et al., 2017) have excellent processing speed and accuracy, which was chosen to identify weld lines.

Weld line recognition and tracking by the inspection robot include the following steps:

- (1) Identifying weld lines from background (surrounding environment);
- (2) Detecting edges and segmenting pixels of weld lines;
- (3) Extracting and fitting centerlines of weld paths;
- (4) Selecting routes and adjusting robot's position to track weld lines.

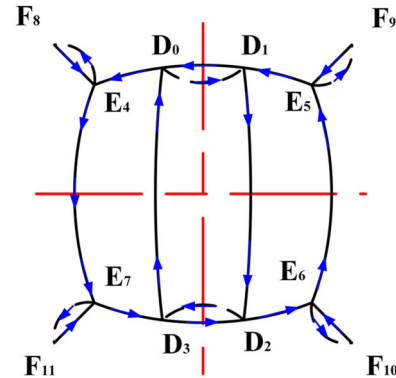
## 5.1 | Network model

Figure 17 shows the basic process of recognizing and extracting weld lines. In the initial stage, weld line images were captured by the camera mounted on the inspection robot. A deep learning network mainly composed of Mask R-CNN was used to identify weld lines from captured images and perform instance segmentation. Subsequently, weld paths were extracted by image processing and the least squares method.

The process of Mask R-CNN for weld line recognition includes feature extraction by CNNs, candidate region processing, RoIAlign layer, classification, regression, and mask generation. At the beginning, a series of CNN layers (such as ResNet50 and ResNet101) were used to extract feature maps of weld line images. In this stage,

feature maps were fused by feature pyramid networks (FPN) to fully utilize the features with different depths.

The feature maps outputted from the backbone network were sent to the region proposal network (RPN). The RPN network generated regions of interest (RoIs). To avoid deviations, the corresponding features of each RoI on the feature maps were extracted by RoIAlign



**FIGURE 14** Running route in the upper pole zone map

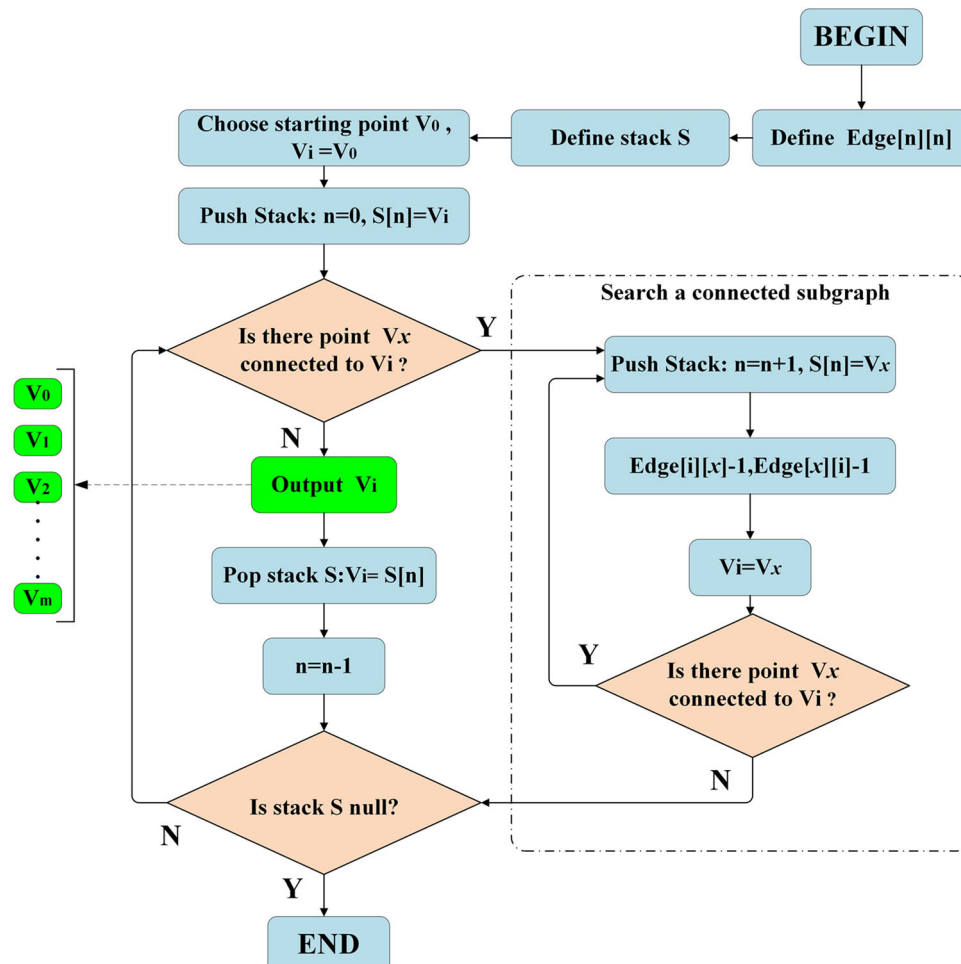


**FIGURE 13** Solution procedure of searching for an Eulerian circuit

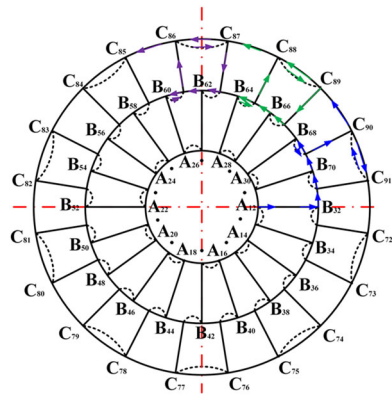


**FIGURE 15** Running route in the middle zone map



**FIGURE 16** Weld line images captured by the inspection robot

with bilinear interpolation. The connected prediction network includes three branches: classification prediction, regression of bounding boxes, and mask generation.

## 5.2 | Training and testing

In total, 1500 weld line images, with  $320 \times 240$  pixels, were collected as a training data set, among which the ratio of single weld lines to intersected weld lines was 3:1. The number of categories in the data set was 2 (representing background and weld line) and the output network was simpler (its depth was 2). In training and testing process, the smaller size could reduce training time and recognition time, but it had little impact on weld path fitting.

The network model was trained on a computer with GeForce RTX2060 for GPU acceleration. Its parameters were set as follows. The initial learning rate of the network was 0.001; the weight attenuation coefficient was 0.0005; the momentum coefficient was 0.8. The curves of the total loss and average accuracy during the

**TABLE 5** Speed-performance and Mask mAP of different instance segmentation algorithms

Algorithms	FPS	Average time (ms)	mAP (%)
PA-Net	4.7	212.8	36.6
RetinaMask	6.0	166.7	34.7
FCIS	6.6	151.5	29.5
Mask R-CNN	8.6	116.3	35.7

training process under the maximum number of iterations of 10,000 are shown in Figure 18.

As shown in Figure 19, testing results of weld line recognition include classification probability, regression boxes and pixel-level mask. The results indicated that the network is suitable for weld line recognition.

After weld lines were identified, image processing, filters, and the least squares method were used to estimate the center line equation  $h(x) = kx + b$ . The position parameters of weld paths, including  $\beta$  and  $d$ , are calculated as follows:

$$\begin{cases} \beta = \arctan k \times 180/\pi \\ d = \frac{y_c - b}{k} - x_c \end{cases} \quad (1)$$

where  $(x_c, y_c)$  is the center coordinate of weld line images.

As shown in Figure 20,  $\beta$  is the drift angle of the robot relative to the weld path and  $d$  is the shortest distance from the weld line to the center of the image. The two parameters were used to correct the robot position to track weld lines. If the captured image includes two intersected weld lines, two center lines will be calculated independently. When the robot reaches the intersected weld points, the next running path will be selected by robot or manually.

## 6 | LABORATORY EXPERIMENTS

To verify the stability of weld line tracking and the feasibility of weld path planning, we conducted experiments with the climbing robot on an experimental platform. As shown in Figure 21, the experimental platform is a cylindrical tank, with a diameter of 4000 mm, a height of 2.8 m, and a thickness of 10 mm. Like spherical tanks, the cylindrical tank was welded from multiple arc-shaped plates.

The laboratory experiments are introduced as follows:

- (1) In weld line tracking experiments, the robot equipped with a camera ran on the vertical wall and automatically recognized and tracked a longitudinal or transverse weld line. With the recorded deviations between the robot and the tracked weld line, the stability of weld line recognition and tracking could be verified.
- (2) In path planning experiments, optimal paths were planned and selected according to the distribution of weld lines on the experimental platform. The moving trajectory and position of the

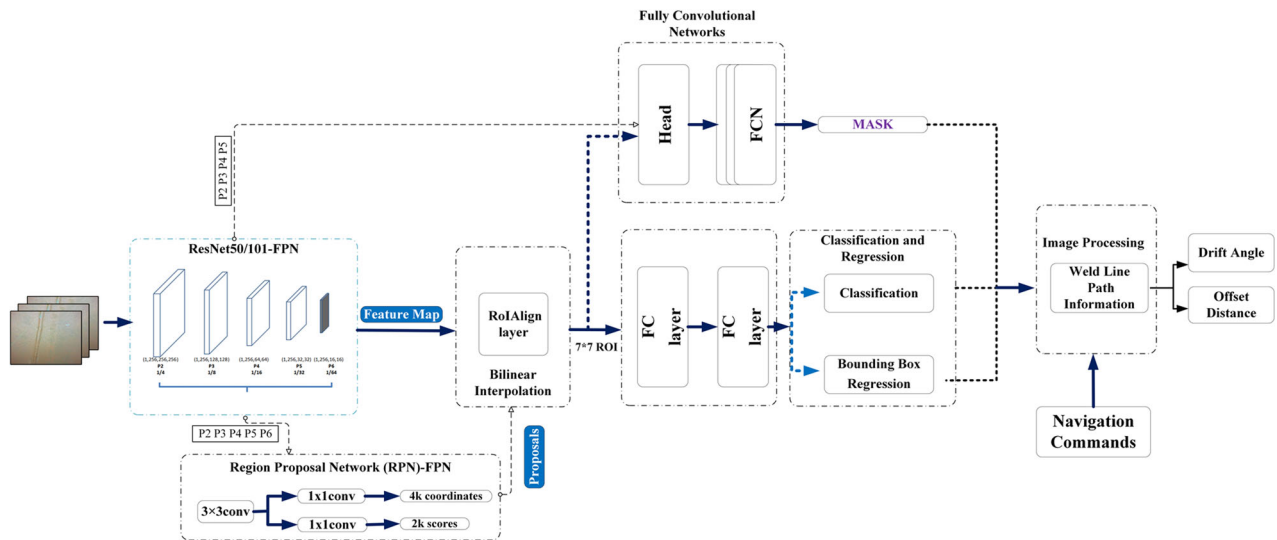


**FIGURE 17** Process of recognizing and extracting weld lines

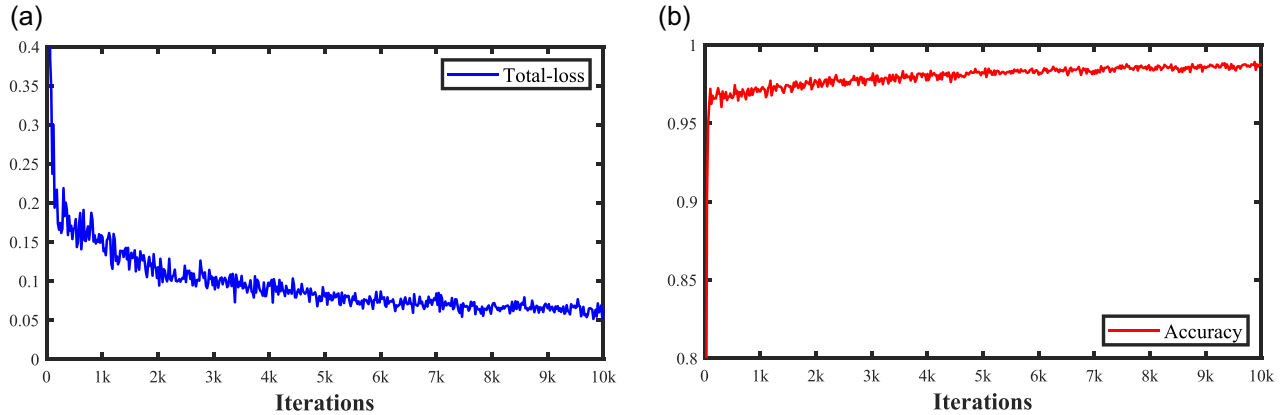


**FIGURE 18** The training process of Mask R-CNN: (a) total loss and (b) average accuracy

robot were dynamically displayed and simulated to verify the feasibility of weld path planning.

## 6.1 | Weld line tracking experiments

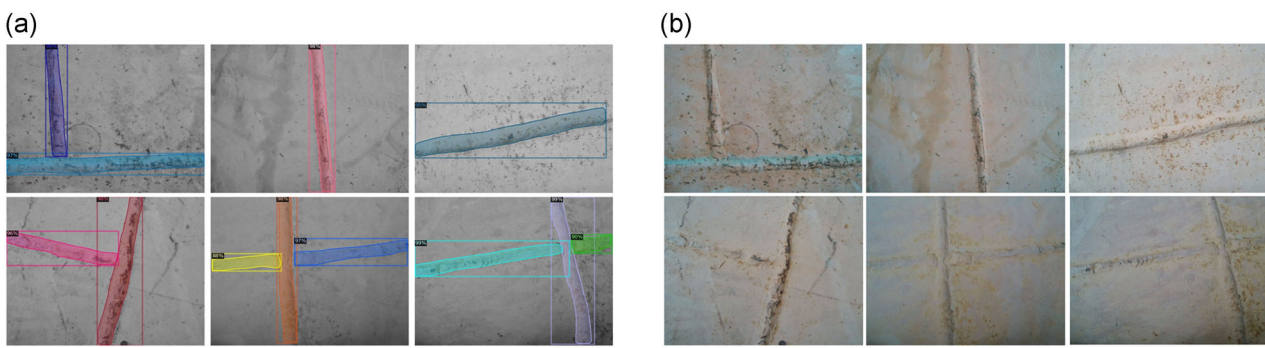
In weld line tracking experiments, the climbing robot attached and ran on the vertical arc-shaped wall of the experimental platform. The weld line images were obtained by the camera installed in the front of the robot. The robot driven by four motors with mecanum wheels could adjust its posture and position faster so as to improve the accuracy and stability of weld line tracking. Figure 22 shows the process of weld line tracking experiments, including longitudinal weld line tracking experiments and transverse weld line tracking experiments.

In the experiments of longitudinal weld line tracking, the robot tracked upward 1.5-m long longitudinal weld line at a speed of

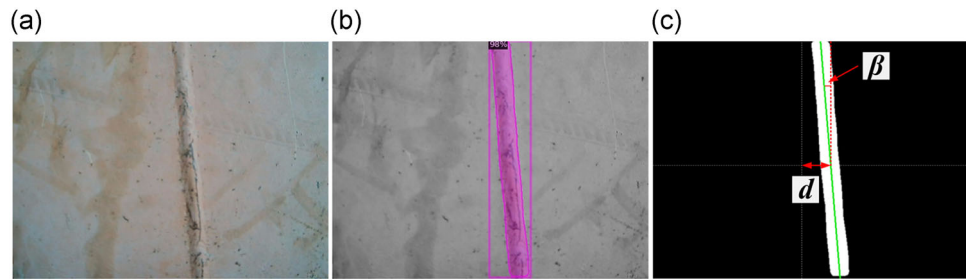
0.06 m/s, then tracked downwards at the same speed. In the experiments of transverse weld line tracking, the robot tracked a transverse weld line in the middle of the experimental platform and the running distance was about 5 m.

Figure 23 shows the real-time recognition results of weld lines, including original images, and a binary weld path images. In the experiments, processing time for each weld image was about 0.2–0.25 s. The results indicated that the robot could successfully identify and extract the weld path.

The changing curves of drift angle  $\beta$  and offset  $d$  in the weld line tracking experiments are shown in Figure 24. To keep the robot moving smoothly, the robot would not adjust its posture until the offset exceeded 10 mm. In the experiments of transverse weld line tracking, the initial deviations of the robot were about 3° in angle and 50 mm in distance. After receiving tracking command, the robot quickly adjusted its posture and corrected the deviations. The maximum offset was -19.4 mm and the drift angle was within ±5°. In the



**FIGURE 19** Testing results of weld line recognition: (a) original weld images and (b) recognized weld images



**FIGURE 20** Weld path extraction: (a) original weld image; (b) recognized weld image; (c) weld path image and position parameters

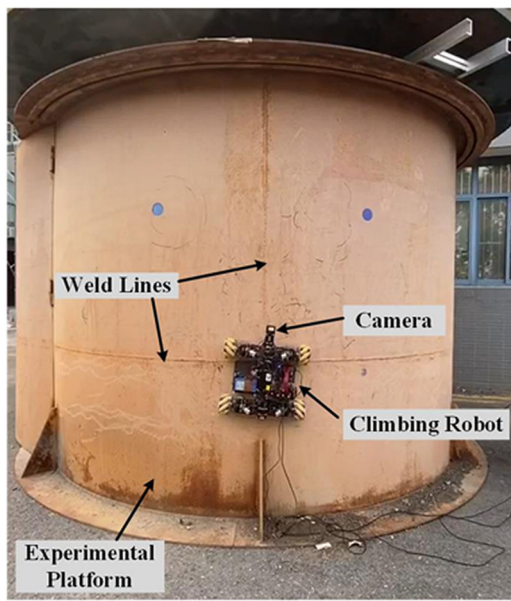


**FIGURE 21** Experimental platform

experiments of longitudinal weld line tracking, the drift angle of the robot was within  $\pm 4^\circ$  and the maximum offset was -18 mm. Experimental results demonstrated that the inspection robot could identify and track weld lines with a maximum offset of  $\pm 20$  mm.

## 6.2 | Path planning experiments

The weld line distribution on the experimental platform is relatively simple and involves a circular weld line and four longitudinal weld lines. Figure 25 shows the 2D distribution map of weld lines. Weld intersections are numbered from 0 to 7. Since Points 1, 2, 3, 5, 6, and 7 are connected by odd edges, repetitive edges ((6,7), (3,4), (1,2) and (4,5)) are added to make the running path be an Euler circuit.

A virtual 3D experimental platform was constructed and weld lines were depicted as several lines according to their actual distribution. In the experiments of path planning, robot's running trajectory was dynamically displayed. When the robot traced a weld line and reached a weld intersection, the next running weld route was chosen according to the planned optimal path, and finally the robot traversed all of weld lines. When the starting point was Point 0, the shortest running path of traversing all weld lines was:  $0 \rightarrow 2 \rightarrow 1 \rightarrow 2 \rightarrow 4 \rightarrow 3 \rightarrow 4 \rightarrow 5 \rightarrow 4 \rightarrow 6 \rightarrow 7 \rightarrow 6 \rightarrow 0$ . As shown in Figure 26, dynamic red lines represent robot's running trajectory; green dots represent visited weld intersections; white dots represent unvisited weld intersections. Experimental results indicated that the robot could complete the shortest path planning to traverse all weld lines on the experimental platform. Based on the weld line tracking status, the real-time running trajectory of the robot could be displayed in the virtual 3D experimental platform.

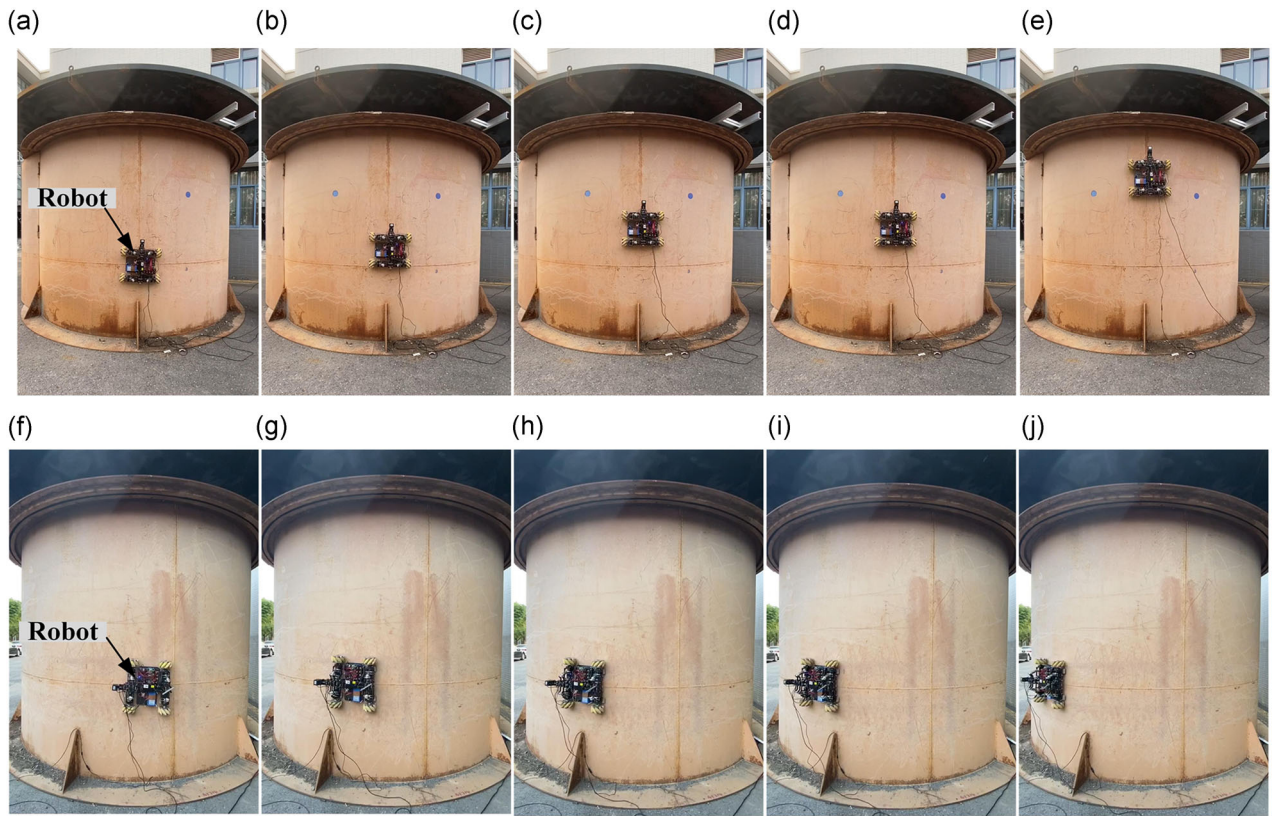


**FIGURE 22** Weld line tracking experiments: (a)–(e) longitudinal weld line tracking experiments and (f)–(k) transverse weld line tracking experiments

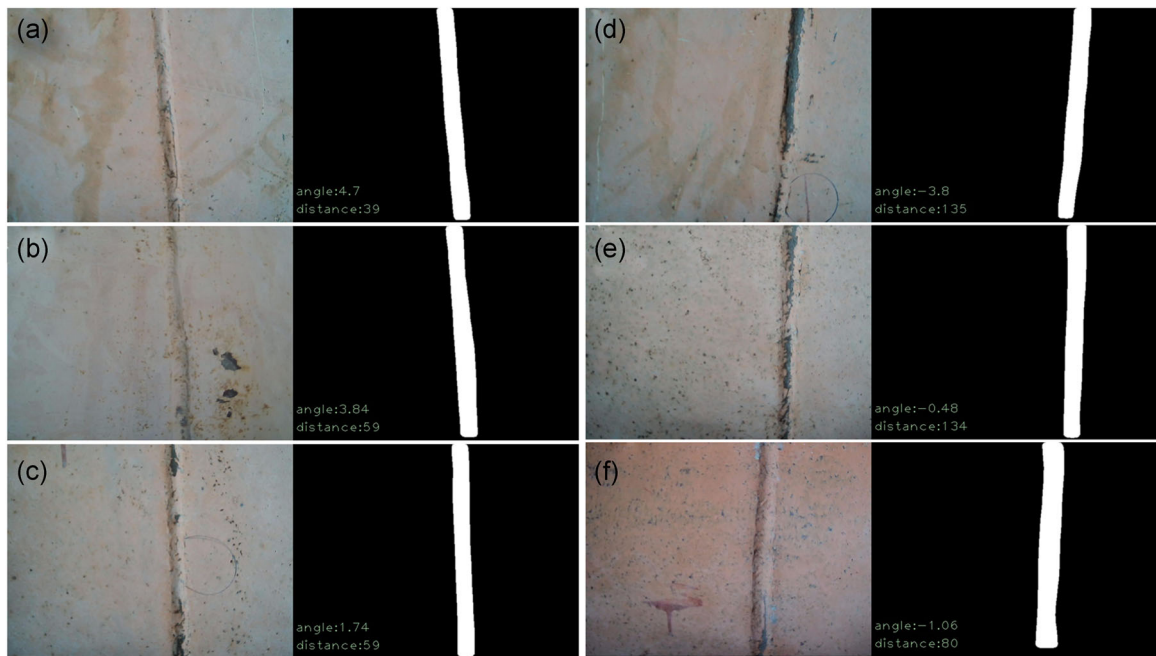


**FIGURE 23** Real-time recognition results of weld lines: (a) angle:  $4.7^\circ$ , distance: 39 pixels; (b) angle:  $3.84^\circ$ , distance: 59 pixels; (c) angle:  $1.74^\circ$ , distance: 59 pixels; (d) angle:  $-3.8^\circ$ , distance: 135 pixels; (e) angle:  $-0.48^\circ$ , distance: 134 pixels; (f) angle:  $-1.06^\circ$ , distance: 80 pixels

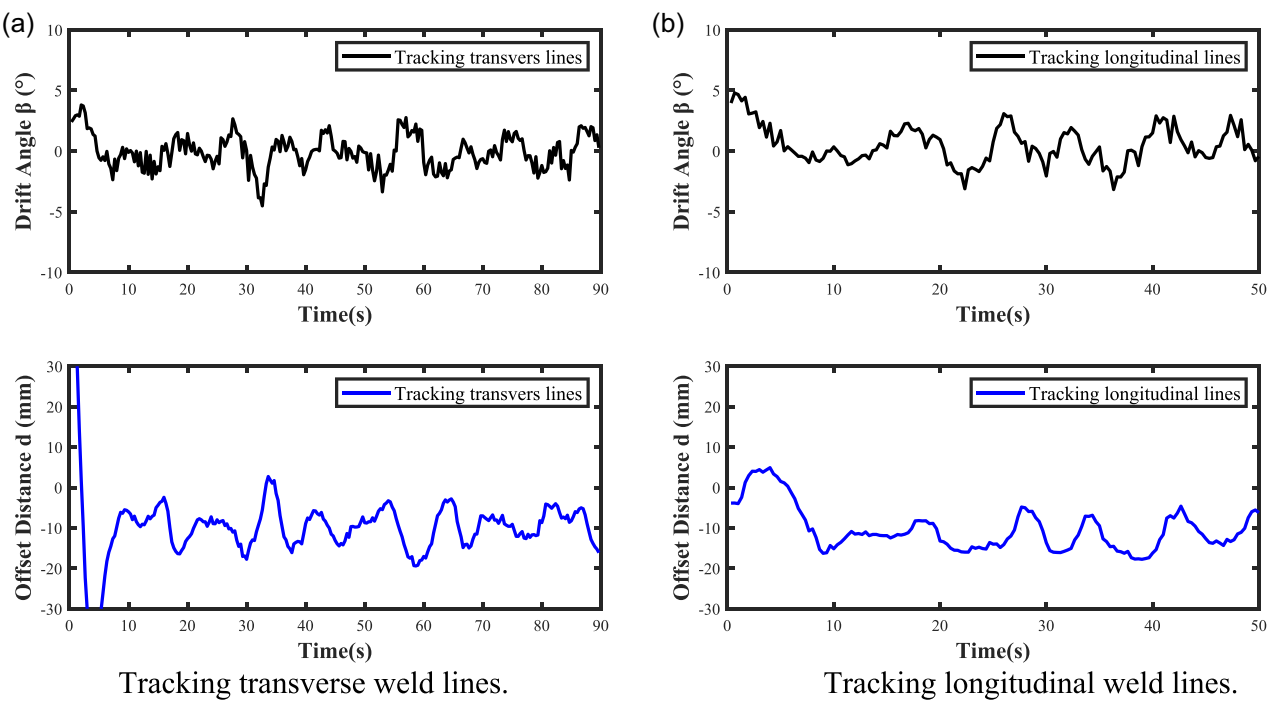


**FIGURE 24** Results of weld line tracking experiments. Tracking weld lines (a) transverse and (b) longitudinal

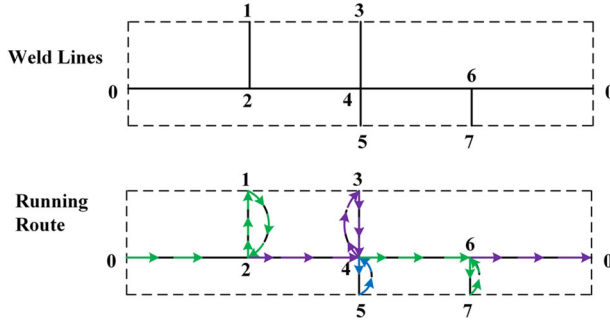


**FIGURE 25** Weld path planning on the experimental platform

## 7 | FIELD TESTS

### 7.1 | Inspection robot system

The schematic of the spherical tank inspection robot system is illustrated in Figure 27. The overall system is composed of a inspection robot and a remote control and monitoring system. In field applications, the robot cooperates with the remote computer to complete the inspection work together. DC power is generated by the lithium battery installed in the robot. The robot system functions include:

- (1) Robot motion control: Workers can control the robot movement through the remote control unit or the remote computer. The robot movement system consists of DC brushless motors, motor drivers, a central controller and wireless module. After receiving the control signal, the robot climbs or stops on the spherical tank.

- (2) Robot positioning and path planning: Benefiting from the robot host computer (GPU is NVIDIA RTX2060), the Mask R-CNN algorithm can quickly recognize weld lines. The encoders are used to record the running distance of tracking weld lines by the robot. After reaching a weld line intersection, the robot will select the next weld line for tracking based on the path planning algorithm. Meanwhile, the robot's position and coordinate are displayed on the remote computer.
- (3) Image monitoring: The real-time images captured by robot's camera and recognition results are sent to the remote computer via the wireless TCP.
- (4) NDT and maintenance: The robot cooperates with the additional mechanisms to detect and maintain weld seams on the spherical tank.

### 7.2 | Real LPG spherical tank

Field tests were carried out to test the practicality and efficiency of the inspection robot in engineering applications. It includes weld line tracking test and path planning test on spherical tanks. As shown in Figure 28, the inspection robot was tested on a real LPG spherical tank. It was built to store propylene in October 2017 in Lianyungang Port, Jiangsu Province, China. It has a volume of  $3000 \text{ m}^3$  and a design pressure of 2.16 MPa. Its total length of weld lines is 455.46 m. Other parameters of the spherical tank are as follows: Q370R material, a diameter of 18 m, a maximum height of 20 m, and a thickness of 49 mm.

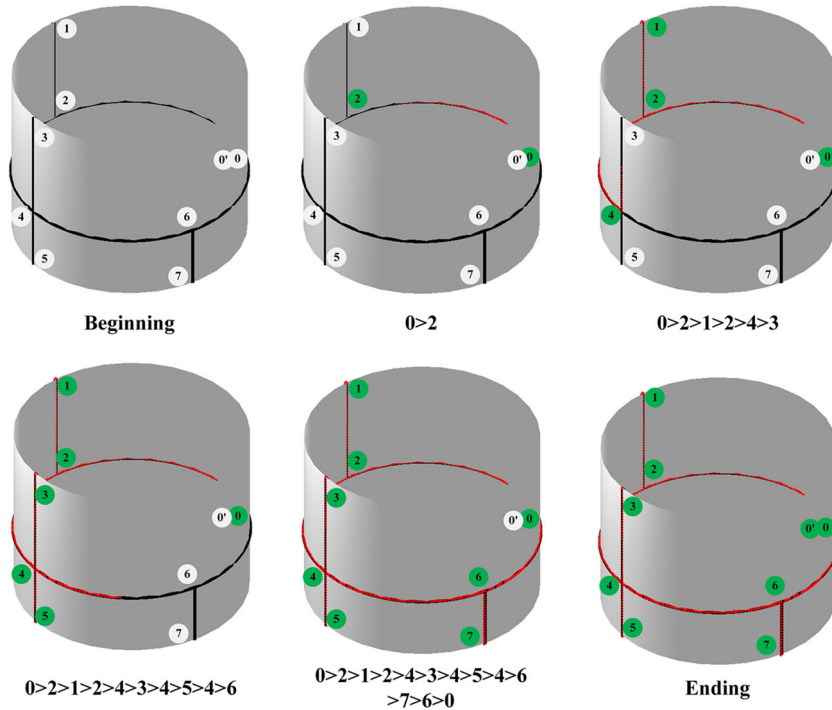


**FIGURE 26** Dynamic path planning in the virtual 3D experimental platform

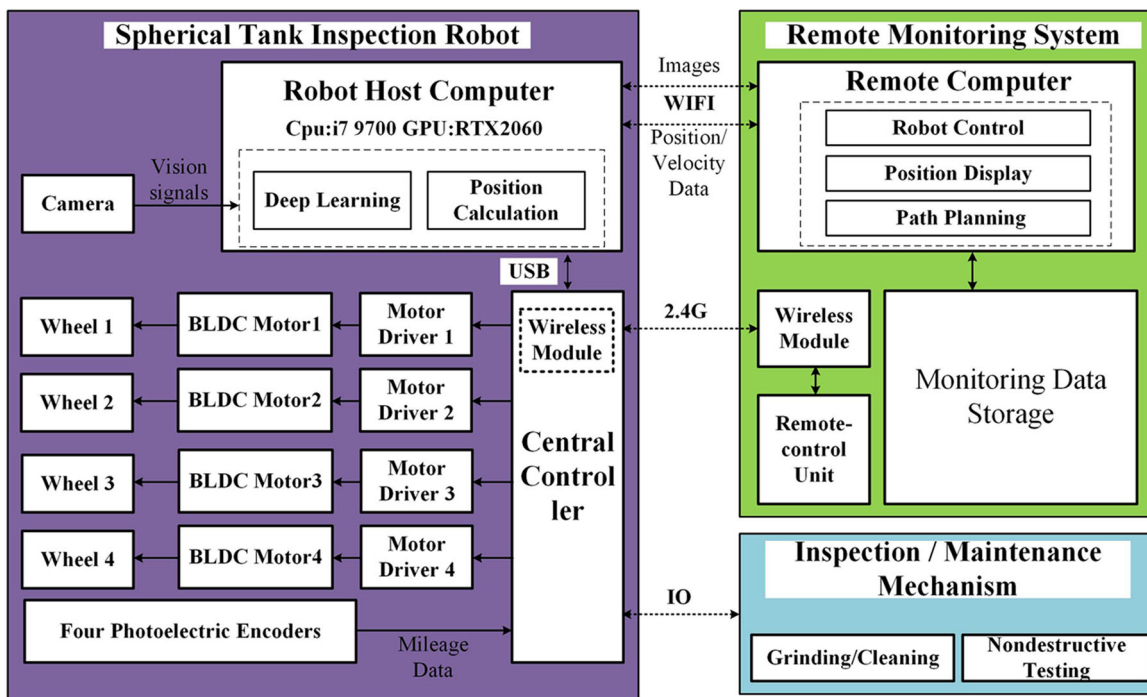


**FIGURE 27** Spherical tank inspection robot system

The spherical tank is a hybrid-type spherical tank with four zones, welded from multiple arc plates. It can be divided into an upper polar zone, an upper temperate zone, an equatorial zone and a lower polar zone. Weld lines of the upper temperate zone and the equatorial zone are distributed along the longitudinal direction and those of the upper polar zone and the lower polar zone are irregular. The number and parameters of weld lines distributed on the spherical tank are indicated in Table 6.

### 7.3 | Real-time tracking weld lines

The weld images of the spherical tank were captured by the robot to expand the training data set of Mask R-CNN. In the test, new 2172 weld images on the surface of the spherical tank were collected. Deep learning is a method of continuous learning. On other different tanks, the training data set of Mask R-CNN will also continue to increase. With more training and learning, the network will be able to

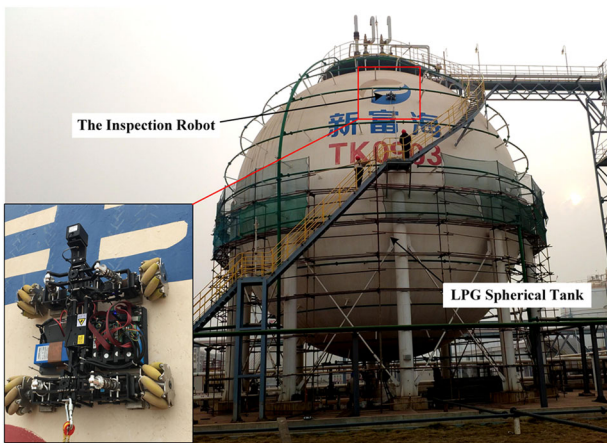


**FIGURE 28** Field tests on LPG spherical tank. LPG, liquefied petroleum gas

recognize more types of weld lines. At present, we have trained more weld images of different spherical tanks.

Figure 29 shows tracking process of weld lines by the robot. The results show that the robot can quickly and effectively identify weld lines and extract weld path information. The average recognition time of each weld image was about 0.2 s and the robot could automatically run along weld lines. When the robot reaches one intersected weld point, the robot will stop and wait for the next running command, the next running route will be selected by robot or manually based on the planned path. In special cases, such as no weld line and unrecognized, the robot can be switch to manual remote control to solve these troubles.

#### 7.4 | Path planning on spherical tanks

To complete the inspection operation within the shortest time, an optimal running route was planned for robot traversing all weld lines on the spherical tank. According to the design parameters of the spherical tank, a virtual 3D spherical tank was constructed for displaying robot's running trajectory. Similar to the 2D weld maps, in the virtual spherical tank, weld intersections and weld lines were depicted as sequential points and lines. Based on the proposed path planning algorithm, optimal running routes were calculated and searched after selecting one point as the starting position of the robot.

When the robot only climbed on and inspected the upper pole zone of the spherical tank, for example, if Point 9 was selected as the starting point, the planned path was obtained as: 9 → 5 → 6 → 10 → 6 → 2 → 3 → 7 → 11 → 7 → 4 → 8 → 4 → 0 → 1 → 0 → 3 → 2 → 1 → 5 → 9. Figure 30 shows the dynamic running trajectory of the robot in the upper pole zone. The robot finally returned to the starting point (Point 9) after traversing all the planned weld paths. Multiple optimal paths with the same total distance may exist, but they are all based on the premise of adding the same repetitive edges. Table 7 shows the comparison of different path planning methods. The results

**TABLE 6** Weld line distribution on the tested spherical tank

Zones	Plates	Weld lines	Length (m)	Sum (m)
Upper polar zone	7	4	1.589	6.356
		4	6.278	25.112
		2	6.759	13.518
Upper circular weld line		1	34.876	34.876
Upper temperate zone	20	20	5.48	109.6
Middle circular weld line		1	49.136	49.136
Equatorial zone	20	20	6.85	137
Lower circular weld line		1	34.876	34.876
Lower polar zone	7	4	1.589	6.356
		4	6.278	25.112
		2	6.759	13.518
<b>Sum (m)</b>				455.46

demonstrated that running distance of robot's path planning is the shortest, which is better than other three manual planning methods.

When the robot inspected all weld lines of the spherical tank, optimal running routes could be planned from any starting point. Some examples of the starting point in different zones of the spherical tank are provided as Table 8.

In the test, the robot's running distance on weld seams was recorded by encoders of four wheels. The starting point, the reached intersection points and the selected weld lines of the robot also be recorded. The real-time position of the robot (on which weld line or which weld intersection) was integrated into the global 3D maps. Figure 31 shows weld path planning and dynamic robot's running trajectory on the virtual spherical tank surface, in which Point 12 was selected as the starting point. Figure 32 shows the field test of the inspection robot on the real 3000-m<sup>3</sup> spherical tank. The simulation and test results indicated that the robot could traverse all weld lines of the spherical tank along the shortest running route.

Running paths planned by workers may include more repeatedly visited weld lines. Especially when a new starting point is selected, the automatic path planning is faster and more flexible. In the field tests, the inspection robot could climb on the surface of the spherical tank stably and track weld lines smoothly. In addition, the shortest running route was automatically planned by the robot. The field tests confirmed the practicability and high efficiency of weld line tracking and path planning with the robot in engineering applications.

## 8 | CONCLUSION

This paper presents a spherical tank inspection robot, which can identify and track weld lines on the shortest running route. With NDT equipment and repair tools, it can be used to inspect and maintain weld seams of spherical tanks. Basically, the robot is

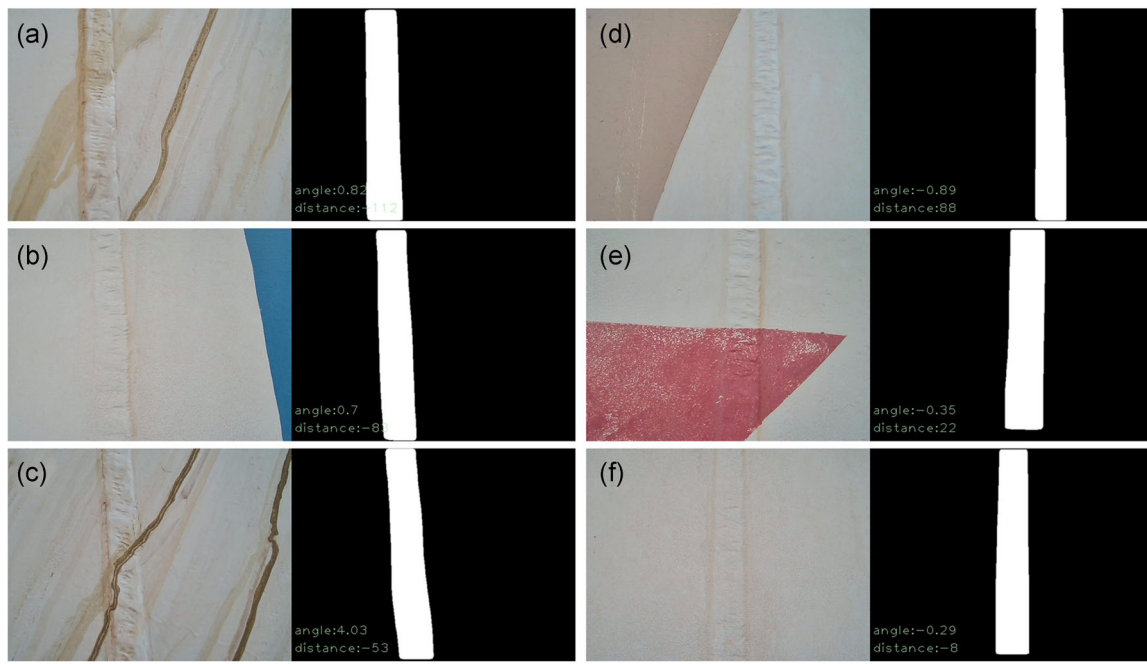


**FIGURE 29** Real-time weld line tracking by the inspection robot on the LPG spherical tank: (a) angle:  $0.82^\circ$ , distance:  $-112$  pixels; (b) angle:  $0.7^\circ$ , distance:  $-83$  pixels; (c) angle:  $4.03^\circ$ , distance:  $-53$  pixels; (d) angle:  $-0.89^\circ$ , distance:  $88$  pixels; (e) angle:  $-0.35^\circ$ , distance:  $22$  pixels; (f) angle:  $-0.29^\circ$ , distance:  $-8$  pixels

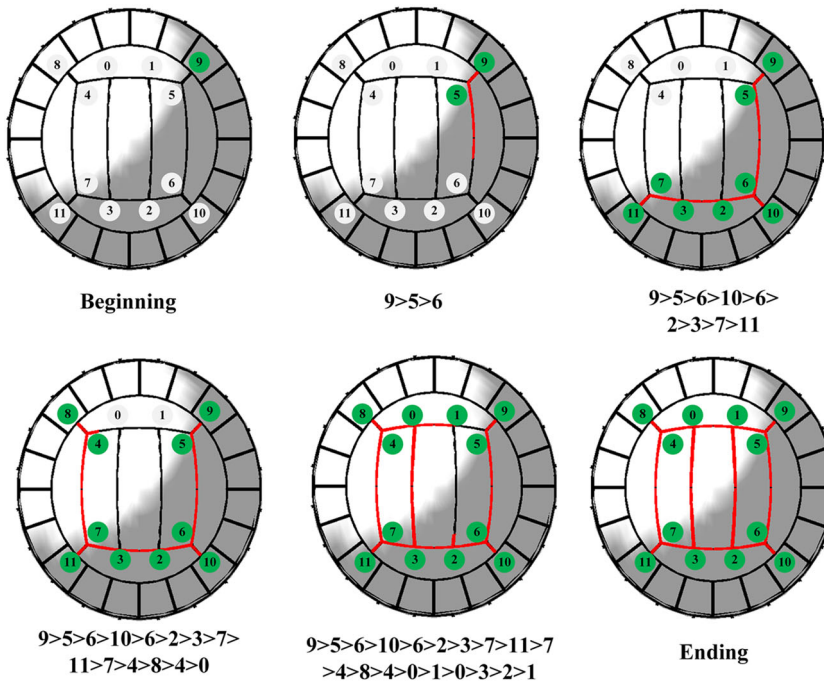


**FIGURE 30** Path planning in the upper pole zone

**TABLE 7** Comparison of different path planning methods

Method	Running route	Length (m)
Robot's path planning	$9 \rightarrow 5 \rightarrow 6 \rightarrow 10 \rightarrow 6 \rightarrow 2 \rightarrow 3 \rightarrow 7 \rightarrow 11 \rightarrow 7 \rightarrow 4 \rightarrow 8 \rightarrow 4 \rightarrow 0 \rightarrow 1 \rightarrow 0 \rightarrow 3 \rightarrow 2 \rightarrow 1 \rightarrow 5 \rightarrow 9$	40.38
Manual path planning 1	$9 \rightarrow 5 \rightarrow 1 \rightarrow 0 \rightarrow 4 \rightarrow 8 \rightarrow 4 \rightarrow 7 \rightarrow 11 \rightarrow 7 \rightarrow 3 \rightarrow 0 \rightarrow 3 \rightarrow 2 \rightarrow 1 \rightarrow 2 \rightarrow 6 \rightarrow 10 \rightarrow 6 \rightarrow 5 \rightarrow 9$	46.65
Manual path planning 2	$9 \rightarrow 5 \rightarrow 6 \rightarrow 2 \rightarrow 3 \rightarrow 7 \rightarrow 4 \rightarrow 0 \rightarrow 1 \rightarrow 5 \rightarrow 6 \rightarrow 10 \rightarrow 6 \rightarrow 2 \rightarrow 1 \rightarrow 0 \rightarrow 3 \rightarrow 7 \rightarrow 11 \rightarrow 7 \rightarrow 4 \rightarrow 8 \rightarrow 4 \rightarrow 0 \rightarrow 1 \rightarrow 5 \rightarrow 9$	56.51
Manual path planning 3	$9 \rightarrow 5 \rightarrow 1 \rightarrow 2 \rightarrow 3 \rightarrow 0 \rightarrow 4 \rightarrow 7 \rightarrow 11 \rightarrow 7 \rightarrow 3 \rightarrow 2 \rightarrow 6 \rightarrow 10 \rightarrow 6 \rightarrow 5 \rightarrow 1 \rightarrow 0 \rightarrow 4 \rightarrow 8 \rightarrow 4 \rightarrow 0 \rightarrow 1 \rightarrow 5 \rightarrow 9$	47.35

**TABLE 8** Robot path planning on 3000-m<sup>3</sup> spherical tank

Zone	Starting point	Planned path
Upper temperate zone	Point 12	12 → 32 → 71 → 70 → 69 → 68 → 69 → 90 → 91 → 90 → 89 → 88 → 89 → 67 → 66 → 65 → 64 → 65 → 88 → 87 → 86 → 87 → 63 → 62 → 61 → 60 → 61 → 86 → 100 → 96 → 99 → 103 → 99 → 95 → 94 → 98 → 102 → 98 → 97 → 101 → 97 → 93 → 94 → 95 → 92 → 93 → 92 → 96 → 100 → 85 → 84 → 85 → 59 → 58 → 57 → 56 → 57 → 84 → 83 → 82 → 83 → 55 → 54 → 53 → 52 → 53 → 82 → 81 → 80 → 81 → 51 → 50 → 49 → 48 → 49 → 80 → 79 → 78 → 79 → 47 → 46 → 45 → 44 → 45 → 78 → 77 → 76 → 77 → 43 → 42 → 41 → 40 → 41 → 76 → 102 → 75 → 74 → 75 → 39 → 38 → 39 → 40 → 16 → 17 → 42 → 43 → 44 → 18 → 19 → 46 → 47 → 48 → 20 → 21 → 50 → 51 → 52 → 22 → 23 → 54 → 55 → 56 → 24 → 25 → 58 → 59 → 60 → 26 → 27 → 62 → 63 → 64 → 28 → 29 → 66 → 67 → 68 → 30 → 31 → 70 → 71 → 91 → 72 → 73 → 74 → 37 → 36 → 37 → 38 → 15 → 14 → 36 → 35 → 34 → 73 → 72 → 33 → 32 → 33 → 34 → 13 → 12 → 13 → 14 → 15 → 16 → 17 → 18 → 19 → 20 → 21 → 9 → 5 → 6 → 10 → 6 → 2 → 3 → 2 → 1 → 5 → 9 → 22 → 23 → 24 → 25 → 26 → 27 → 28 → 29 → 30 → 31 → 11 → 7 → 4 → 8 → 4 → 0 → 1 → 0 → 3 → 7 → 11 → 12
Upper polar zone	Point 8	8 → 4 → 7 → 11 → 31 → 30 → 68 → 69 → 90 → 91 → 90 → 89 → 88 → 89 → 67 → 66 → 65 → 64 → 65 → 88 → 87 → 86 → 87 → 63 → 62 → 61 → 60 → 61 → 86 → 100 → 96 → 99 → 103 → 99 → 95 → 94 → 98 → 102 → 98 → 97 → 101 → 97 → 93 → 94 → 95 → 92 → 93 → 92 → 96 → 100 → 85 → 84 → 85 → 59 → 58 → 57 → 56 → 57 → 84 → 83 → 82 → 83 → 55 → 54 → 53 → 52 → 53 → 82 → 81 → 80 → 81 → 51 → 50 → 49 → 48 → 49 → 80 → 79 → 78 → 79 → 47 → 46 → 45 → 44 → 45 → 78 → 77 → 76 → 77 → 43 → 42 → 41 → 40 → 41 → 76 → 102 → 75 → 74 → 75 → 39 → 38 → 39 → 40 → 16 → 17 → 42 → 43 → 44 → 18 → 19 → 46 → 47 → 48 → 20 → 21 → 50 → 51 → 52 → 22 → 23 → 54 → 55 → 56 → 24 → 25 → 58 → 59 → 60 → 26 → 27 → 62 → 63 → 64 → 28 → 29 → 66 → 67 → 68 → 69 → 70 → 71 → 91 → 72 → 73 → 74 → 37 → 36 → 37 → 38 → 15 → 14 → 36 → 35 → 34 → 73 → 72 → 33 → 34 → 13 → 14 → 15 → 16 → 17 → 18 → 19 → 20 → 21 → 9 → 5 → 9 → 22 → 23 → 24 → 25 → 26 → 27 → 28 → 29 → 30 → 31 → 70 → 71 → 32 → 33 → 32 → 12 → 13 → 12 → 11 → 7 → 3 → 2 → 6 → 10 → 6 → 5 → 1 → 2 → 3 → 0 → 1 → 0 → 4 → 8
Equatorial zone	Point 88	88 → 89 → 90 → 91 → 90 → 69 → 68 → 69 → 70 → 71 → 91 → 72 → 73 → 72 → 33 → 34 → 35 → 73 → 74 → 75 → 74 → 37 → 36 → 37 → 38 → 39 → 75 → 102 → 98 → 97 → 101 → 97 → 93 → 92 → 96 → 100 → 96 → 99 → 103 → 99 → 95 → 94 → 95 → 92 → 93 → 94 → 98 → 102 → 76 → 77 → 76 → 41 → 40 → 41 → 42 → 43 → 77 → 78 → 79 → 78 → 45 → 44 → 45 → 46 → 47 → 79 → 80 → 81 → 80 → 49 → 48 → 49 → 50 → 51 → 81 → 82 → 83 → 82 → 53 → 52 → 53 → 54 → 55 → 83 → 84 → 85 → 84 → 57 → 56 → 57 → 58 → 59 → 85 → 100 → 86 → 87 → 86 → 61 → 60 → 61 → 62 → 63 → 87 → 88 → 89 → 67 → 66 → 67 → 68 → 30 → 31 → 70 → 71 → 32 → 33 → 32 → 12 → 13 → 34 → 35 → 36 → 14 → 15 → 38 → 39 → 40 → 16 → 17 → 42 → 43 → 44 → 18 → 19 → 46 → 47 → 48 → 20 → 21 → 50 → 51 → 52 → 22 → 23 → 54 → 55 → 56 → 24 → 25 → 58 → 59 → 60 → 26 → 27 → 62 → 63 → 64 → 65 → 66 → 29 → 28 → 29 → 30 → 31 → 11 → 7 → 11 → 12 → 13 → 14 → 15 → 16 → 17 → 18 → 19 → 20 → 21 → 9 → 5 → 6 → 10 → 6 → 2 → 3 → 7 → 4 → 8 → 4 → 0 → 3 → 2 → 1 → 0 → 1 → 5 → 9 → 22 → 23 → 24 → 25 → 26 → 27 → 28 → 64 → 65 → 88.
Lower polar zone	Point 94	94 → 95 → 99 → 103 → 99 → 96 → 100 → 86 → 87 → 86 → 61 → 60 → 61 → 62 → 63 → 87 → 88 → 89 → 88 → 65 → 64 → 65 → 66 → 67 → 89 → 90 → 91 → 90 → 69 → 68 → 69 → 70 → 71 → 91 → 72 → 73 → 72 → 33 → 34 → 35 → 73 → 74 → 75 → 74 → 37 → 36 → 37 → 38 → 39 → 75 → 102 → 98 → 102 → 76 → 77 → 76 → 41 → 40 → 41 → 42 → 43 → 77 → 78 → 79 → 78 → 45 → 44 → 45 → 46 → 47 → 79 → 80 → 81 → 80 → 49 → 48 → 49 → 50 → 51 → 81 → 82 → 83 → 82 → 53 → 52 → 53 → 54 → 55 → 83 → 84 → 85 → 84 → 57 → 56 → 57 → 58 → 59 → 60 → 26 → 27 → 62 → 63 → 64 → 65 → 66 → 29 → 28 → 29 → 30 → 31 → 11 → 7 → 11 → 12 → 13 → 14 → 15 → 16 → 17 → 18 → 19 → 20 → 21 → 9 → 5 → 6 → 10 → 6 → 2 → 3 → 7 → 4 → 8 → 4 → 0 → 3 → 2 → 1 → 0 → 1 → 5 → 9 → 22 → 23 → 24 → 25 → 58 → 59 → 85 → 100 → 96 → 92 → 95 → 94 → 98 → 97 → 101 → 97 → 93 → 92 → 93 → 94.

composed of an adjustable body, shock-absorbing suspensions, magnetic adsorption units, and mecanum wheels. It can be adapted to spherical tanks with different diameters through the adjustable body and elastic suspensions. In this study, a path planning method was proposed to search for the optimal running route which covers all weld lines of spherical tanks with the shortest total distance. The distribution of weld lines on spherical tanks was analyzed and discussed. Also, the corresponding 2D weld maps were prepared for path planning. By adding appropriate repetitive edges in the 2D maps, the shortest Eulerian circuit was depicted. With the improved Fleury algorithm, the optimal running route was solved.

Based on Mask R-CNN and image processing, the robot could recognize weld lines successfully. Laboratory experiments were conducted to test the stability of weld line tracking performance and the feasibility of weld path planning. The experimental results indicated that the inspection robot could identify and track weld lines, with a maximum offset of 20 mm and a maximum angular deviation of 5°. In the simulation experiments of path planning, robot's running trajectory was dynamically displayed in the virtual 3D experimental platform. Starting from any point on the experimental platform, the shortest running route could be planned to traversal all weld lines.

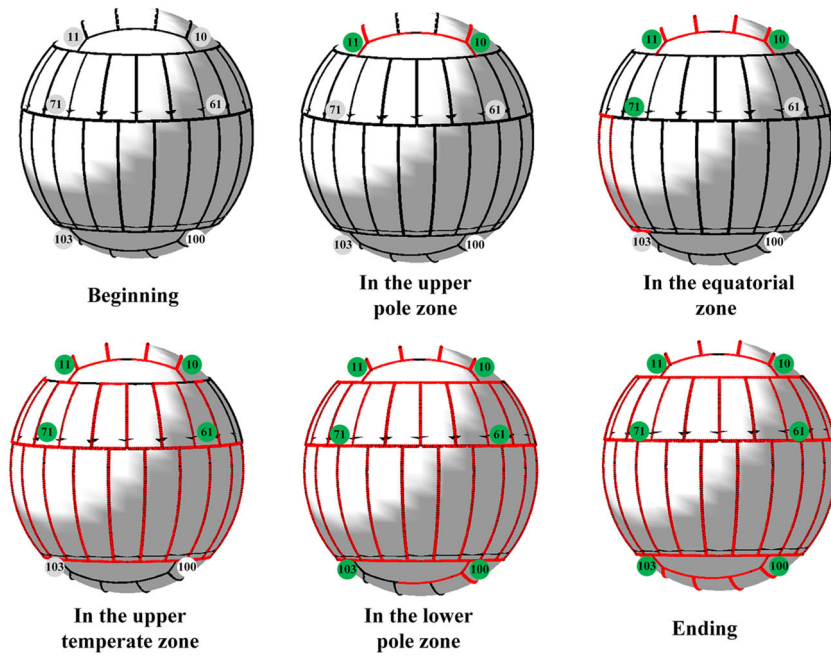


**FIGURE 31** Path planning on the spherical tank surface

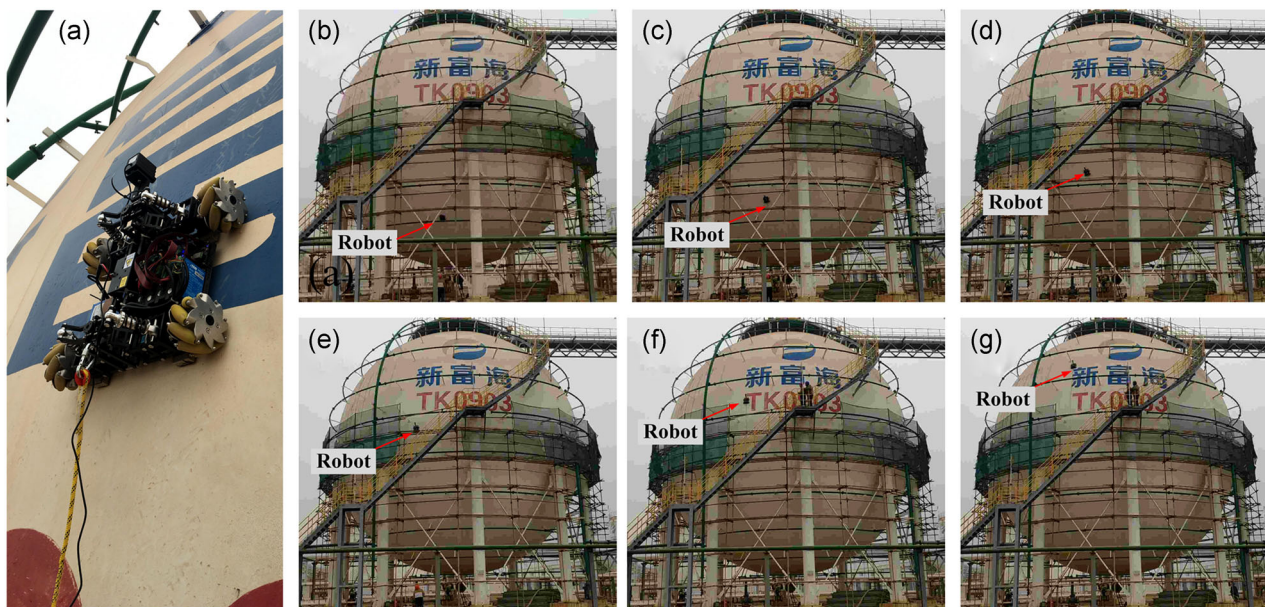


**FIGURE 32** Field test on the 3000-m<sup>3</sup> spherical tank: (a) inspection robot; (b)-(g) robot running process

Furthermore, we introduced a 3000 m<sup>3</sup> spherical tank as an application example to discuss local and global path planning of weld lines for the designed robot. The results of the field tests verified the practicality and stability of the inspection robot. The intelligent robot system can improve the efficiency of inspection operation greatly. In the future, we will verify the path planning and weld recognition method with more spherical tanks to optimize the performance of the robotic system. Equipped with different instruments and tools on the robot, more tests will be carried out to expand its application scope.

#### ACKNOWLEDGMENTS

The authors wish to thank Dr. Cunlei Tu from Special Equipment Safety Supervision Inspection Institute of Jiangsu Province for their support in facilitating and performing field tests, Feng Huang from Southeast University for helping us design the suspension mechanism. This study was supported by the National Prevention Key Technology Project for Serious and Major Accidents in Work Safety of China, under Grant jiangsu-0002-2017AQ and the Science and Technology Project of Quality and Technical Supervision Bureau of Jiangsu Province, China, under Grant KJ175933.

## DATA AVAILABILITY STATEMENT

The data that support the findings of this study are available from the corresponding author upon reasonable request.

## ORCID

Jie Li  <http://orcid.org/0000-0001-8380-3340>

## REFERENCES

- Da Veiga, R. S., de Oliveira, A. S., de Arruda, L. V. R., & Junior, F. N. (2016). *Localization and navigation of a climbing robot inside a LPG spherical tank based on dual-LIDAR scanning of weld beads* (pp. 161–184). Springer International Publishing.
- Ding, Y., Sun, Z., & Chen, Q. (2019). Non-contacted permanent magnetic absorbed wall-climbing robot for ultrasonic weld inspection of spherical tank. *MATEC Web of Conferences*, 269, 2013.
- Eiselt, H. A., Gendreau, M., & Laporte, G. (1995). Arc routing problems, part I: The Chinese postman problem. *Operations Research*, 43, 231–242.
- Espinosa, R. V., de Oliveira, A. S., de Arruda, L. V. R., & Junior, F. N. (2015). Navigation's stabilization system of a magnetic adherence-based climbing robot. *Journal of Intelligent & Robotic Systems*, 78, 65–81.
- Faruq Howlader, M. O., & Sattar, T. P. (2015). Novel adhesion mechanism and design parameters for concrete wall-climbing robot. In *2015 SAI Intelligent Systems Conference* (pp. 267–273). IEEE.
- Fernández, R., González, E., Feliú, V., & Rodríguez, A. G. (2010). A wall climbing robot for tank inspection. An autonomous prototype. In *2010 36th Annual Conference on IEEE Industrial Electronics Society* (pp. 1424–1429). IEEE.
- Fu, C., Shvets, M., & Berg, A. C. (2019). RetinaMask: Learning to predict masks improves state-of-the-art single-shot detection for free. *arXiv preprint arXiv: 1901.03353*. <http://arxiv.org/abs/1901.03353>
- Günther, J., Pilarski, P. M., Helfrich, G., Shen, H., & Diepold, K. (2016). Intelligent laser welding through representation, prediction, and control learning: An architecture with deep neural networks and reinforcement learning. *Mechatronics*, 34, 1–11.
- He, K., Gkioxari, G., Dollar, P., & Girshick, R. (2017). Mask R-CNN. *IEEE Transactions on Pattern Analysis and Machine Intelligence*, 42, 386–397.
- Kim, B., & Cho, S. (2019). Image-based concrete crack assessment using mask and region-based convolutional neural network. *Structural Control and Health Monitoring*, e2381.
- Kim, J., & Lee, S. (2016). A vehicular positioning with GPS/IMU using adaptive control of filter noise covariance. *ICT Express*, 2, 41–46.
- La, H. M., Dinh, T. H., Pham, N. H., Ha, Q. P., & Pham, A. Q. (2019). Automated robotic monitoring and inspection of steel structures and bridges. *Robotica*, 37, 947–967.
- Leon-Rodriguez, H., Hussain, S., & Sattar, T. (2012). A compact wall-climbing and surface adaptation robot for non-destructive testing. In *2012 12th International Conference on Control, Automation and Systems* (pp. 404–409). IEEE.
- Li, B., Ushiroda, K., Yang, L., Song, Q., & Xiao, J. (2017). Wall-climbing robot for non-destructive evaluation using impact-echo and metric learning SVM. *International Journal of Intelligent Robotics and Applications*, 1, 255–270.
- Li, J., Feng, H., Tu, C., Jin, S., & Wang, X. (2019). Design of inspection robot for spherical tank based on Mecanum wheel. In *2019 Far East NDT New Technology & Application Forum* (pp. 218–224). IEEE.
- Li, J., & Wang, X. S. (2016). Novel omnidirectional climbing robot with adjustable magnetic adsorption mechanism. In *2016 23rd International Conference on Mechatronics and Machine Vision in Practice* (pp. 1–5). IEEE.
- Li, Y., Qi, H., Dai, J., Ji, X., & Wei, Y. (2016). Fully Convolutional Instance-aware Semantic Segmentation. In *2017 IEEE Conference on Computer Vision and Pattern Recognition (CVPR)*. IEEE.
- Liang, G., Wang, S., Tu, C., & Wang, X. (2016). Existing weld seam recognition and tracking based on sub region neutral network. In *2016 23rd International Conference on Mechatronics and Machine Vision in Practice*. IEEE.
- Liang, G., Zheng, K., Tu, C., Wang, S., & Wang, X. (2017). Existing weld seam recognition based on image processing. In *2017 Far East NDT New Technology & Application Forum* (pp. 181–186). IEEE.
- Lin, C., Huang, Y., Chen, S., Hsu, Y., & Lin, Y. (2018). The application of deep learning and image processing technology in laser positioning. *Applied Sciences*, 8, 1542.
- Liu, S., Qi, L., Qin, H., Shi, J., & Jia, J. (2018). Path aggregation network for instance segmentation. In *2018 IEEE/CVF Conference on Computer Vision and Pattern Recognition* (pp. 8759–8768). IEEE.
- Oliveira, A. L. C., Silva, M. F., & Barbosa, R. S. (2010). Architecture of an wheeled climbing robot with dynamic adjustment of the adhesion system. In *IEEE 8th International Symposium on Intelligent Systems and Informatics* (pp. 127–132). IEEE.
- Ren, S., He, K., Girshick, R., & Sun, J. (2017). Faster R-CNN: Towards Real-Time Object Detection with Region Proposal Networks. *IEEE Transactions on Pattern Analysis and Machine Intelligence*, 39, 1137–1149.
- Rout, A., Deepak, B. B. V. L., & Biswal, B. B. (2019). Advances in weld seam tracking techniques for robotic welding: A review. *Robotics and Computer-Integrated Manufacturing*, 56, 12–37.
- Sassi, P., Tripicchio, P., & Avizzano, C. A. (2019). A smart monitoring system for automatic welding defect detection. *IEEE Transactions on Industrial Electronics*, 66, 9641–9650.
- Sogi, T., Kawaguchi, Y., Morisaki, H., Ohkawa, K., Kai, N., & Hayakawa, H. (2000). Inspection robot for spherical storage tanks. In *2000 26th Annual Conference of the IEEE Industrial Electronics Society. IECON 2000. 2000 IEEE International Conference on Industrial Electronics, Control and Instrumentation. 21st Century Technologies* (pp. 393–398). IEEE.
- Spies, M., Rieder, H., Dillhöfer, A., Schmitz, V., & Müller, W. (2012). Synthetic aperture focusing and time-of-flight diffraction ultrasonic imaging—past and present. *Journal of Nondestructive Evaluation*, 31, 310–323.
- Tâche, F., Fischer, W., Caprari, G., Siegwart, R., Moser, R., & Mondada, F. (2009). Magnebike: A magnetic wheeled robot with high mobility for inspecting complex-shaped structures. *Journal of Field Robotics*, 26, 453–476.
- Teixeira, M. A. S., Santos, H. B., Dalmedico, N., de Arruda, L. V. R., Neves, F., & de Oliveira, A. S. (2018). Intelligent environment recognition and prediction for NDT inspection through autonomous climbing robot. *Journal of Intelligent & Robotic Systems*, 92, 323–342.
- Tu, C., Li, X., Li, J., Wang, X., & Sun, S. (2017). Bilateral laser vision tracking synchronous inspection robotic system. In *2017 Far East NDT New Technology & Application Forum* (pp. 207–215). IEEE.
- Wang, S., & Wang, X. (2016). Existing weld seam recognition based on sub-region BP\_Adaboost algorithm. In *2016 23rd International Conference on Mechatronics and Machine Vision in Practice (M2VIP)*. IEEE.
- Wang, Z., Zhang, K., Chen, Y., Luo, Z., & Zheng, J. (2017). A real-time weld line detection for derusting wall-climbing robot using dual cameras. *Journal of Manufacturing Processes*, 27, 76–86.
- Zhang, B., & Peng, J. (2012). Uncertain programming model for Chinese postman problem with uncertain weights. *Industrial Engineering and Management Systems*, 11, 18–25.
- Zhang, L., Ke, W., Ye, Q., & Jiao, J. (2014). A novel laser vision sensor for weld line detection on wall-climbing robot. *Optics & Laser Technology*, 60, 69–79.

- Zhang, L., Ye, Q., Yang, W., & Jiao, J. (2014). Weld Line detection and tracking via spatial-temporal cascaded hidden markov models and cross structured light. *IEEE Transactions on Instrumentation and Measurement*, 63, 742–753.
- Zheng, K., Li, J., Tu, C., & Wang, X. (2016). Two opposite sides synchronous tracking X-ray based robotic system for welding inspection. In *2016 23rd International Conference on Mechatronics and Machine Vision in Practice* (pp. 1–5). IEEE.

**How to cite this article:** Li, J., Jin, S., Wang, C., Xue, J., & Wang, X. (2022). Weld line recognition and path planning with spherical tank inspection robots. *Journal of Field Robotics*, 39, 131–152.  
<https://doi.org/10.1002/rob.22042>